POLITECNICO DI TORINO

Collegio di Ingegneria Meccanica, Aerospaziale e dell'Autoveicolo

Master of Science Course in Mechanical Engineering

Politecnico di Torino

Master of Science Thesis

Numerical Investigation on Cavitation Occurrence in a 2/2 Proportional Valve

Academic Supervisor
Prof. Massimo Rundo

Company Supervisor
Eng. Aniello Valiante

Candidate
Cansu Duman

December 2024

Ringraziamenti

Innanzitutto, vorrei ringraziare il professor Rundo per avermi dato la possibilità di svolgere questa tesi sotto la sua supervisione. Durante questo periodo, è stato sempre disponibile per rispondere alle mie domande e per discutere in generale, e non posso sottolineare abbastanza quanto sia importante per una tesista avere una supervisione di questo tipo. È stata una grande opportunità per me che mi ha permesso di ampliare le mie conoscenze in un campo leggermente nuovo e di crescere come ingegnere. Un ringraziamento va sicuramente anche all'Ing. Valiante, che è stato molto gentile e sempre pronto ad aiutare, ampliando la mia visione sulle cose dalla prospettiva di un ingegnere. Un altro ringraziamento va ai ragazzi del laboratorio, in particolare a Giuseppe, con cui è stato piacevole scambiare delle chiacchiere sui risultati delle partite del fine settimana ogni lunedì mattina (a mezzogiorno).

Concludo con questa tesi un grande capitolo della mia vita, il mio percorso accademico, che mi ha regalato tanti momenti di gioia, tristezza, stress ed entusiasmo che mi hanno fatto crescere, permettendomi di incontrare persone straordinarie lungo il cammino.

İlk olarak, anne ve babama, her zaman yanımda olduklarını hissettirdikleri, sınırsız destekleri, ben belki de daha ilkokuldayken bu yüksek lisansa gelebilmem için kendilerinden fedakârlık yaparak kenara koydukları ve bana kattıkları hayat vizyonları için teşekkür ederim.

Bu dünyadaki en sevdiğim insan olan abime, bana verdiği sonsuz güvenin ve anlayışın yanı sıra her zaman önden giderek bana yol açtığı için, çünkü eminim ki ilk olmak onun için çok zor olmuştur ama onun sayesinde ben bunu hiçbir zaman hissetmedim. Keşke onun da kendi gibi bir abisi olsaydı. Kardeş!

Ringrazio la mia famiglia italiana, per avere un cuore così grande da poter accettare una figlia e sorella che non conoscevano prima. Nonostante mi sia aggiunta a loro ormai sette anni fa, sono stati gentilissimi ad accogliermi e non lasciarmi più. Mi sento davvero fortunata ad avere due famiglie così belle.

Grazie a Lorenzo, che mi è vicino, rendendomi forte, tranquilla ma soprattutto felice. Credo sia giusto che come quando ci siamo conosciuti all'inizio della magistrale, adesso che la concludo, ci sia tu al mio fianco, che per me sei una delle cose più belle di questa magistrale. Ti voglio bene.

Giray'a, her anlamıyla gerçek bir dost olduğu, herhangi bir konuda yardımına danışabileceğimi bildiğim ve tabii ki de daha kim bilir nicelerine gideceğimiz Avrupa gezilerimiz için teşekkür ederim.

Son olarak kemik kadrom Ahmet ve Mertkan'a, yüksek lisansımı eğlenceli kılan panke akşamları, yeni dans hareketleri, sonsuz boyuttaki şaka kapasiteniz, mizah anlayışınız ama en önemlisi de bu kadar farklı olmamıza rağmen çok iyi arkadaşlar olduğunuz için teşekkür ederim.

Abstract

Cavitation is a major issue in hydraulic systems that degrades the life of the valve by damaging its walls and the piping downstream through implosions of vapor bubbles. Over the years, many studies have been conducted to raise a solution to such problem. Eventually, the solution can be divided into two categories: changing the process parameters or modifying the valve itself.

This thesis focuses on the second type of solution where a prototype valve designed by HTS S.r.l. is analyzed and compared in terms of vapor presence to a commercial 2/2 proportional valve that is prone to cavitation using the commercial computational fluid dynamics (CFD) software ANSYS Fluent, while keeping the process parameters constant.

The presence of cavitation in these two valves is evaluated by two different perspectives to cover the principle working conditions of the system: opening of the valve and direction of the flow. In total, four openings (5, 10, 20 and 40-millimeter) and two directions of flow (converging and diverging) have been investigated. In addition, the performance of a new valve housing that has been developed to prevent cavitation from extending to the outlet section has been evaluated.

Keywords: cavitation, proportional valve, CFD

Contents

List of Figures

1 Introduction

1.1 Cavitation

Cavitation is observed when the local pressure of the fluid flow goes below its vapor pressure caused by a pressure drop that is mainly due to an increase in the velocity of the fluid, causing vapor bubbles to form. When the bubbles travel to a zone with higher pressure they implode by an impinging jet that passes through the bubble at constant temperature, that causes intense heat and high-pressure shockwaves. In Figure 1.1, the difference between cavitation and boiling is shown on a pressure versus temperature diagram.

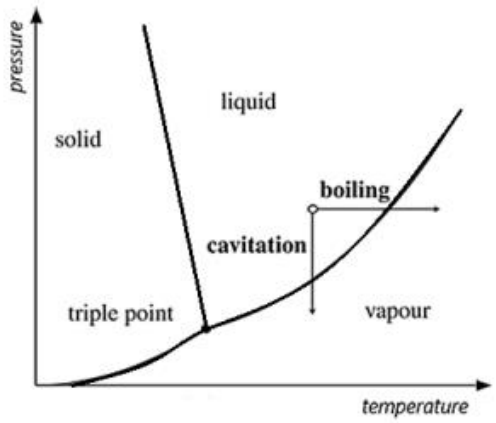

Figure 1.1 Cavitation and boiling representation (Krella, 2023)

When it happens near a solid surface, cavitation leads primarily to erosion, and to pitting corrosion, together with high noise and vibration which reduce the efficiency of the system. It can be seen in any system that involves fluids; however, it is observed mostly in pumps, propellers, and valves as depicted in Figure 1.2. Cavitation causes irreversible damage to components thus reducing cavitation is a highly popular research topic amongst the fluid dynamics field.

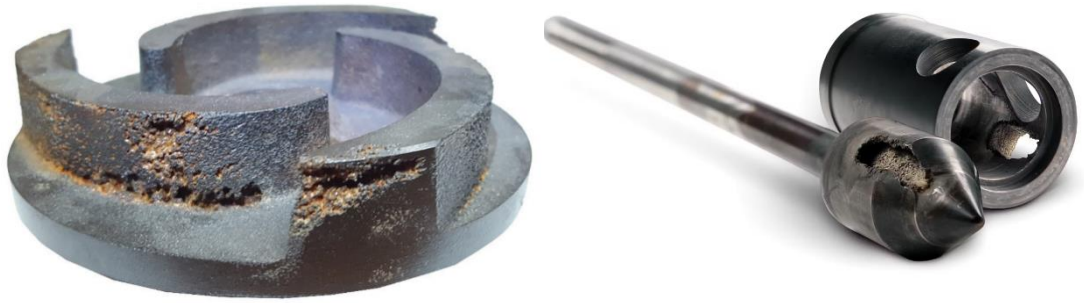

Figure 1.3 Cavitation on a pump (left) and on a valve (right) (Pokharel, 2022 and Arasu, 2020)

Cavitation erosion is a progressive process that can be divided into four stages, shown in Figure 1.3. Incubation (early stage) where the material surface is first exposed to the fluid. Microcracks may be seen at this stage, but they are rather localized and not so significant in terms of degradation. Thus, no material loss is observed. The second stage, accumulation, is where progressive damage is observed as the pits are deepened and cracks start to link up. Material loss rate increases and reaches its maximum in this period. In the deceleration stage, cavitation continues to occur, however, it is less damaging due to the altered surface characteristics during the second stage. In this stage the surface may respond to cavitation by creating a rougher surface, oxide layers and so on. Thus, the material removal decelerates although the damage still occurs. In the final stage, steady state, the erosion rate reaches an

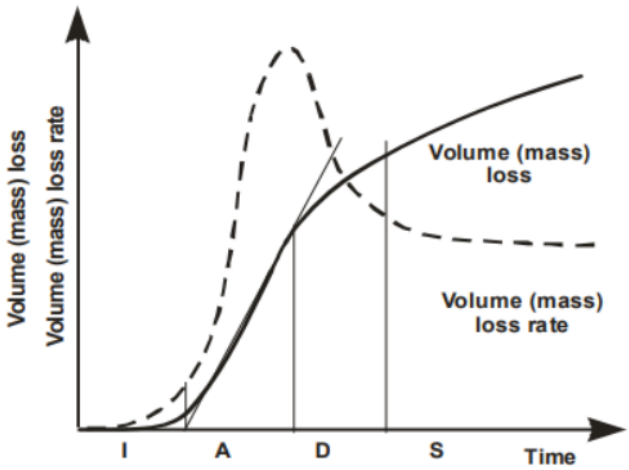

Figure 1.2 Cavitation erosion evaluation over time (Zakrzevska, 2019)

equilibrium where cavitation erosion is balanced by the surface resistance, and it becomes easier to predict.

The solution to cavitation can be divided into two categories: changing the working conditions of the valve (external solution) and changing the characteristics of the valve (internal solution). Before making modifications to the valve geometry, the valve material should be investigated in terms of its susceptibility to cavitation. Cavitation erosion is mainly linked to material hardness, but also to its ductility, impact energy, fatigue strength and material structure. It is seen that the phase transformation from Feγ to Feα' shows great resistance to cavitation observed in 304 steels [1]. Thus, austenite fraction and cavitation reduction are inversely proportional. This is due to the increase in hardness after the transformation. In Figure 1.4, the response of different material structures to cavitation are given. Many solutions may be attributed to improving the hardness of the material and can be analyzed in five categories: thermos-chemical treatment (carburizing and surface hardening), mechanical treatment (shot peening, cold working, friction stir), laser processing, physical vapor coating deposition and finally HVOF/HVAF (High Velocity Oxygen/Air Fuel coating deposition). Usually, increasing the back pressure and using fillets

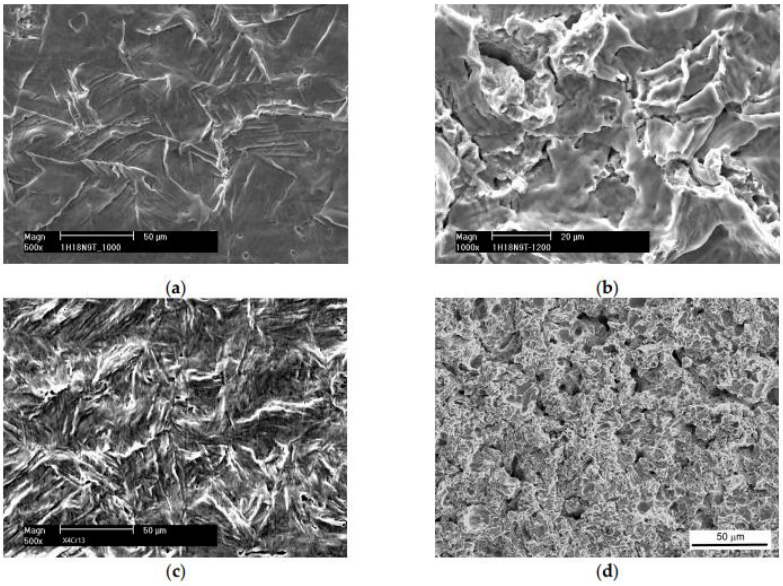

Figure 1.4 Acceleration period cavitation erosion damage on the surface of (a, b) Cr18Ni9Ti austenitic stainless steel; (c, d) X4Cr13 martensitic stainless steel (Krella, 2023)

instead of sharp edges in the minimum area of passage between the valve seat and the poppet is verified to reduce cavitation. These solutions will be further discussed in the literature review section.

1.2 Computational Fluid Dynamics (CFD)

Computational fluid dynamics allow simulating a system of interest in the virtual environment, without the need of expensive and tedious experiments, to predict the flow dynamics using numerical analysis based on conservation of mass, momentum and energy equation (depending on the problem) that describe velocity, pressure, temperature and other flow parameters. The numerical analysis can be done using different methods: finite-element (FEM), finite-difference (FDM) and finite volume method (FVM). The equations in space and time are discretized to approximate solutions at the mesh points. CFD simulations save time especially on design problems, since the procedure of developing a new design, testing and revising according to the results may be time consuming. For this study, commercial software Fluent (ANSYS, Inc., Canonsburg, PA) has been utilized. Ansys Fluent, as the numerical method, uses the finite-volume method that is known for its success in fluid flow problems. In the FVM, the conservation laws are applied to the domain that is divided into control volumes, as shown in Figure 1.5. The differential equations are approximated by discretizing the integrals over each control volume, so that a system of algebraic equations is achieved that can be solved numerically. Then, the equations are

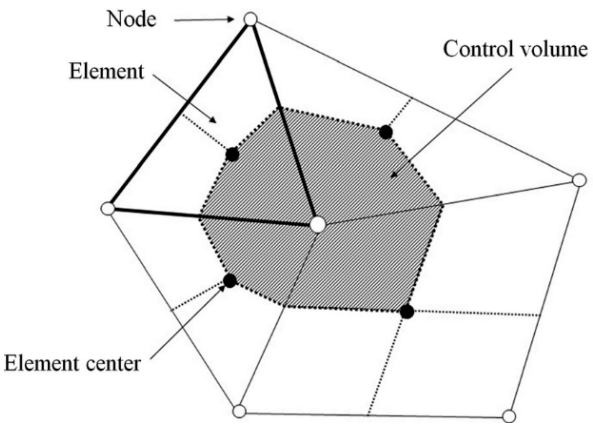

Figure 1.5 Representation of a control volume in the finite volume method (Kim, 2015)

solved for each cell to obtain the flow properties in an iterative manner, with the help of solver methods such as SIMPLE, SIMPLEC and so on.

1.3 Control valves

Control valves are widely used in the industries such as oil and gas plants, water treatment, HVAC systems, food processing due to their reliability, ease of operation and efficiency. Flow control valves are used to regulate the flow process parameters such as pressure, temperature, and flow rate by adjusting the vertical distance between the poppet and the valve seat, hence the opening of the valve. In Figure 1.6, examples of such valves are provided.

Figure 1.6 Pressure (left) and flow rate (right) regulating control valve (Eaton, Misumi)

The position of the poppet is adjusted using an electronic controller, a positioner and the actuator of the valve so that the desired process parameters are controlled and maintained. The main components of flow control valves are shown in Figure 1.6 and explained below.

- The **valve body** is the housing of the valve that keeps together all the remaining components and connects the valve to the piping of the circuit.
- The **actuator** moves the poppet of the valve to control the valve's opening and closing either manually (with the help of a lever or handwheel) or automatically (powered by electricity, hydraulics or pneumatics). Electric and pneumatic actuators are preferred for automated applications while pneumatic actuation is the most

common type for applications in throttling where three types of actuators can be named: piston, rotary vane and spring-and-diaphragm.

- The **valve plug (poppet)** ensures complete closure of the valve when in contact with the valve seat. It may translate or rotate depending on the type of the valve to allow the fluid passage either partially or fully.
- The **valve seat** creates a seal together with the plug to ensure the prevention of the flow without leaks. Seats can be sharp-edged or conical, depending on the application. Generally, conical seats last longer due to the larger contact area. In sharp edged seats, through time, the poppet and the seat wear off due to the point contact resulting in a decrease in valve's life.
- **Valve stem** is a connecting component between the actuator and the valve plug. It transmits the force coming from the actuator to open or close the valve.
- Automated valves include also a **positioner**, to ensure that the poppet has been raised or lowered the right amount.

Figure 1.7 Control valve components (Don, 2022)

1.3.1 2/2 proportional valve

The flow rate is controlled by a 2/2 (two-way, two-position) solenoid activated proportional valve with the help of a control signal. The valve has only one inlet and one outlet port and includes open loop control. The proportionality is between the control signal and the opening of the valve. The flow rate is regulated by the amount of opening of the valve, rather than being just an on/off type, that permits fine-tuning for flow rate and pressure. Proportional valves have a wide range of applications including hydraulic systems, but also in chemical processes for dosing of liquids, as well as the food and beverage industry, press systems, molding machines and medical applications. The activation of the valve is depicted in Figure 1.8.

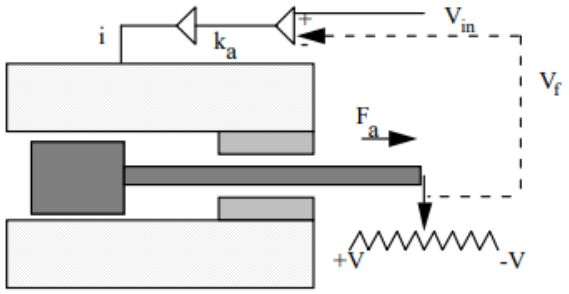

Figure 1.8 Proportional solenoid with position feedback (BTP Hydraulics)

The working principle of the valve can be described as follows: A control signal energizes the solenoid that creates an electromagnetic force that moves the poppet. The balancing force is a sum of friction, flow force and inertial forces. Without feedback control, the hysteresis would be too high, which is a common problem in proportional valves. With the movement of the poppet, the amount of fluid passing through the minimum area is managed, since the orifice area is changed. As mentioned before, the position of the poppet and the control signal are proportional. When the signal increases, the poppet is further elevated to permit the passage, instead the reduction of the signal results in a contraction of the orifice. The valve is returned to its normally closed position with the help of a spring or a hydraulic force, as the control signal weakens or stops. Proportional valve and its symbol are provided in Figure 1.9.

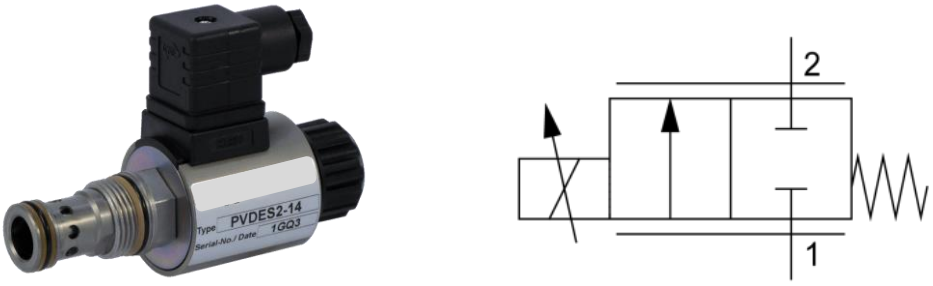

Figure 1.9 2/2 proportional valve (left) and its symbol (right) (Weber-Hydraulik)

The fluids used in the valves can be classified based on their water content. The valve that is analyzed in this study uses a fluid of HFA/HFB/HFC type. The risk of fire and environmental concerns affect the choice of fluid.

- **HFA Fluids:** Oil in water emulsions that contain 95% water and 5% oil. They show excellent fire resistance, however, they have limited lubrication with respect to oil-based fluids.
- **HFB Fluids:** Water in oil emulsions that contain 40% water and 60% oil. They offer better lubrification than HFA type, but they are less resistant to fire.
- **HFC Fluids:** Water-glycol solutions with 45% water and 55% glycol. This type of working fluid offers better lubrification than both HFA and HFB, thus they are more suitable for high-pressure hydraulic systems. Attention must be given to the material to be used to produce the valve, to guarantee that it can resist the chemical properties of glycol for corrosion and wear issues.

1.4 Literature review

Cavitation is a popular research topic in the fluid dynamics area. Many experimental and numerical studies have been conducted to understand the cavitation dynamics and find solutions to reduce or eliminate this destructive phenomenon. Han et al. [2], studied the effects of cavitation in water hydraulic systems, since they are more critical with respect to the oil hydraulic systems due to elevated water vapor pressure. Three seat geometries of a hydraulic poppet valve have been presented: sharp edged, chamfered and two-stage throttle.

It has been found that the two-stage throttle valve seat, because of its pressure compensation effect, had a minor intensity of the vapor phase. Furthermore, the cone angle of the best geometry has been investigated and it has been observed that as the cone angle increases, it results in a higher velocity gradient, in favor of cavitation occurrence. Moreover, as the opening of the valve increases, zones with low pressure expand. Back pressure is found to be helpful in this sense that prevents cavitation from such expansion inside the valve. Bernad et al. [3], found that as the fluid inlet pressure increases, the damage done by cavitation will be more severe as the energy available for such damage is higher. They have conducted a single phase (liquid) flow and a two phase (liquid-vapor) flow and showed that the vortex formation of the velocity streamline contours agrees, as well as the zones defined inside the cavity radius. Thus, one can predict where cavitation might happen using just the single-phase flow simulation. Oshima et al. [4], conducted an experimental study on hydraulic poppet valves, as they evaluated cavitation effects on flow rate, noise level and pressure distribution on two valves with sharp-edged and chamfered seats in both converging and diverging flow. They conclude the study by stating that sharp edged seat is better in terms of unwanted effects, apart from erosion, and has a higher discharge coefficient. In addition, converging flow induces a lower discharge coefficient than diverging flow. Cavitation promotes choking phenomenon inside the valve. Amirante et al. [5], did both experimental and numerical analysis using a hydraulic, proportional directional valve to investigate the effects of cavitation on flow rate and flow force, as the valve opening is varied. As a result, it is found that flow rate worsens with cavitation. Also, if an open loop control system is desired to be implemented, the variation of discharge pressure would result in high errors in poppet position, since the flow force is highly varied depending on the pressure. Habibnejad et al. [6], studied the cavitation reduction numerically simulating a globe valve with an oblique perforated cartridge. It is known that when the pressure drop occurs around the conical area of the valve, it results in a high replacement cost, since the valve itself must be changed. To resolve this issue, the idea is to translate the pressure drop area to the cartridge, with the help of small holes that create a secondary pressure drop zone. In total, four models have been investigated: without the cartridge, cartridge with radial holes, cartridge with holes facing upwards and cartridge with holes facing downwards. It is

proposed to use cartridge since the desired effect is obtained and cavitation shifted from valve inner components and the configuration with downward facing holes is preferred because the fluid flow is directed away from the discharge area at first, and then travels to where the plug and seat are, creating a further pressure drop. Yuan et al. [7], focused on the cavitation-vortex interaction, and found that they are strongly correlated. Cavitation is observed repeatedly at the center of the vortex. In addition, cavitation began forming after a large-scale eddy appearance and the first cavitating vortex ring has an elliptical profile and through time transforms into a circular shape. Xu et al. [8], optimized the design of a hydraulic relief valve to obtain an anti-cavitation valve port structure. Optimization is done by adding jet orifices to the valve core and sharp-edged grooves around the valve seat. A parametric study was conducted where the variables were radius of the jet, the jet angles, and the position of the jet orifices. Objective functions were chosen as average pressure and flow rate in the valve port. Wu et al. [9], focused on reducing noise caused by cavitation in a cartridge pilot-operated relief valve. It is found that the cavitation appears in three main zones: valve core, valve sleeve and outlet flow channel. Cavitation formed at the outlet section has a lower intensity compared to other zones. In addition, in the valve sleeve and core section, cavitation is formed due to separation from the wall of the fluid at high speed, while at the outlet, it is formed due to vortices created due to jets near the outlets. Thus, the jet angle is changed to increase the distance between the jet and the wall and the annular groove on the spool is found to be effective on reducing the cavitation near the spool wall, while cavitation around the sleeve appeared to be difficult to deal with. Dastane et al. [10], worked with both single and multiphase flows and used experimental data to validate their study in cavitating venturi. It is stated that the single-phase simulations greatly overpredict the flow rate for a given pressure drop, compared to the experimental data. A similar trend is observed for maximum velocity and turbulent kinetic energy. In this case, also negative pressure values have been observed, since the cavitation model is not enabled. This causes the pressure downstream the conical zone to further decrease without any limit, also below the vapor pressure since phase change is not considered. Thus, there is no energy lost to phase change and rather it is completely converted into kinetic energy. The paper goes on to conclude that although single-phase flow simulation cannot provide accurate data

predicting the size of cavitation, it still can be used to evaluate the presence of cavitation in design problems due to its computationally inexpensive nature. On the other hand, Ferrarese et al. [11], developed a new method to predict incipient cavitation with single-phase flow model. To overcome the limitation of not being able to predict the flow rate correctly, the paper suggests increasing the pressure interval used in the simulation, by the difference between the minimum pressure value that is observed throughout the domain and the vapor pressure of the fluid, so that no negative pressure is observed.

1.5 Thesis outline

The aim of this study is to analyze two models of a 2/2 proportional valve in terms of cavitation presence with the help of Computational Fluid Dynamics (CFD) software, Ansys Fluent, using single phase flow simulations. Although a multiphase flow model is more accurate in terms of predicting the intensity of cavitation, as well as the flow rate, considering the number of simulations need to be done to complete the study, single phase flow simulation is enough to fulfill the requirements of this study, since a multiphase simulation requires much more computational time. However, a multiphase simulation with cavitation model enabled has been conducted to validate the work that has been done with single-phase simulations. The first valve is a commercial one that is commonly used in industry, while the second valve is developed by the company HTS S.r.l., that aims to reduce the cavitation issue to increase the efficiency of the system. The two valves will be compared in terms of percentage of vapor fraction to evaluate if the prototype valve can indeed reduce cavitation. In section 1, an introduction to the concepts that are dealt with and methods that have been used is done. In the second section, the required knowledge to perform the numerical analysis of this study has been provided with its key concepts. Before the CFD analysis, a 0D analysis has been done on the commercial software Simcenter AMESim, to validate the results to be obtained. In section 3, all the results obtained are presented and discussed, mainly in three aspects: effect of valve opening, effect of flow direction and effect of valve geometry. The conclusion of the conducted study and the future work are presented in the fourth section. References are provided in the fifth section.

2 Method of Numerical Simulation

2.1 0D analysis

The preliminary analysis of the valve is done using commercial software Simcenter AMESim. Firstly, the valve was simulated using two of the components in hydraulic component design library, namely, poppet with conical and sharp-edged seat seen in Figure 2.1. As the poppet geometry changes depending on the opening of the valve, two different simulations have been conducted between zero to 20-millimeter opening and 20 to 40-millimeter opening, where the first port is connected to the outlet pressure, second port to the inlet pressure and third and fourth ports to zero force sources.

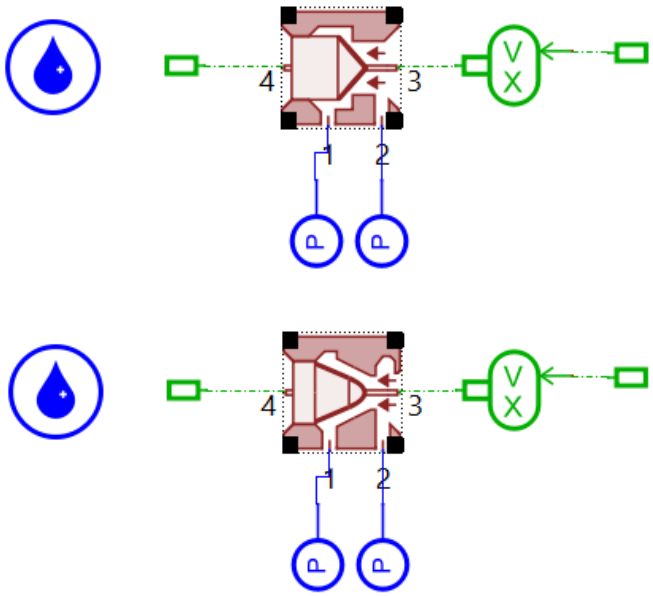

Figure 2.1 Poppet with conical and sharp-edged seat configurations

However, since the poppet and seat geometries are quite complex with respect to the model already available, the outcome of the simulation was not agreeing with the actual geometry. Hence, the valve has been simulated as an orifice for two different cases: pressure inlet-pressure outlet and volume flow inlet-pressure outlet that will be referred to as Case P-P

and Case VFR-P respectively. The reason for doing so is that the valve is limited to a volumetric flow rate of 2500L/min, and it is seen that such value is exceeded for 20 and 40-millimeter openings. The minimum area between the valve poppet and the seat has been calculated from the technical drawings for each corresponding opening, shown in Figure 2.2. The results are presented in Table 1.

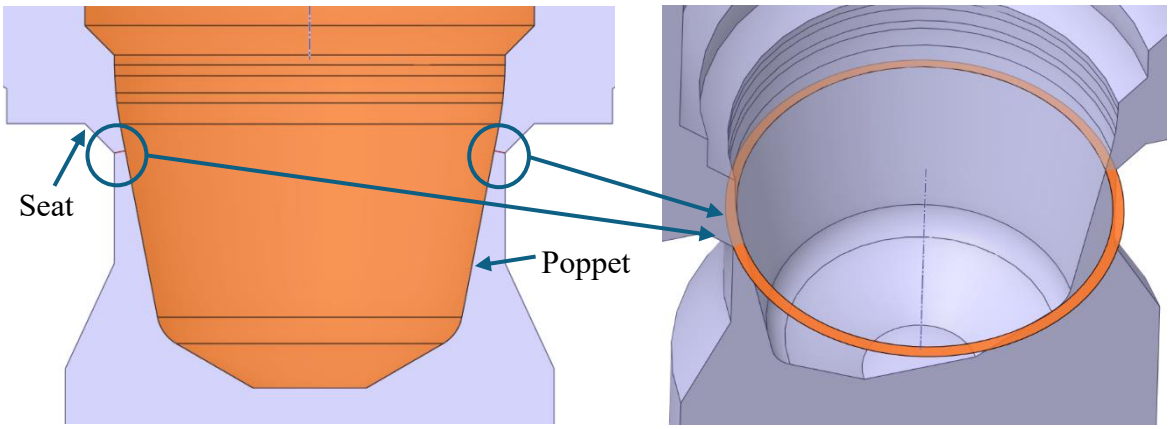

Figure 2.2 Minimum area between the poppet and the seat

Table 1 Flow passage area of different openings of the poppet

Opening [mm]	**5**	**10**	**20**	**40**
Flow passage area [mm^2]	34.78	139.6	354.7	1256.64

The hydraulic orifice is connected to two pressure ports for inlet and outlet. A constant input signal of value 1 is provided to the valve. The working fluid is water at room temperature. The sketches for both cases are provided in Figure 2.3.

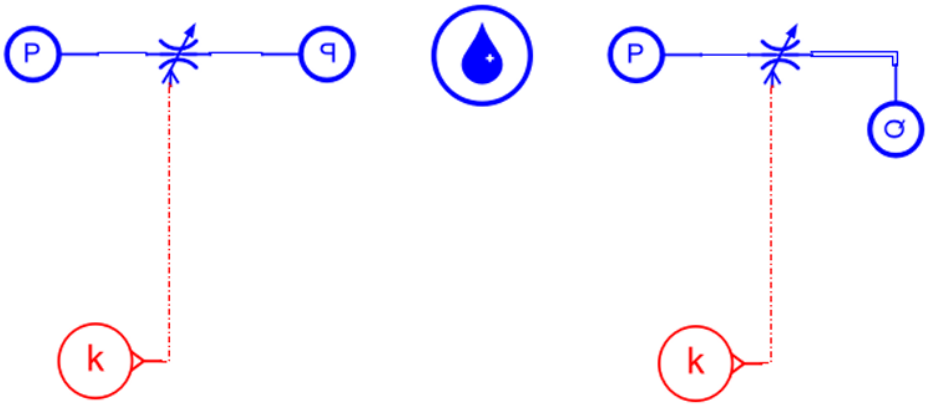

Figure 2.3 Case P-P: Pressure Inlet-Pressure Outlet (left) and Case VFR-P: Volume Flow Inlet-Pressure Outlet (right)

AMESim is used to calculate the discharge coefficient for both cases using Equation (1).

$$Q = C_d A \sqrt{\frac{2\Delta P}{\rho}} \tag{1}$$

$$C_d = \frac{Q_{actual}}{Q_{theoretical}} \tag{2}$$

Where Q is the volumetric flow rate in m^3/s, C_d is the discharge coefficient, A is the minimum flow area across the orifice in m^2, ΔP is the pressure difference upstream and downstream of the orifice in Pa.

Discharge coefficient is a dimensionless number that relates the theoretical flow rate to the actual flow rate that passes across a flow restriction, derived from Bernoulli's principle. Theoretical flow rate is an indicator for an ideal case where there are no losses due to friction

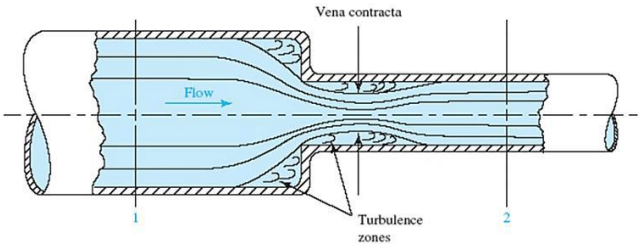

Figure 2.4 Vena contracta effect (Haase, 2017)

or turbulence. Discharge coefficient is affected by factors such as turbulence, orifice geometry, and flow contraction. Mainly, when "vena contracta" effect is observed downstream of the orifice, the discharge coefficient is highly affected as less flow passes from the restriction than that is predicted by Bernoulli's Law. Vena contracta is used to describe a point downstream of the constriction where the fluid flow is at its smallest in terms of cross-sectional area and reaches its highest velocity. Orifice geometry and flow contraction are also related to this concept, as sharp edges induce flow separation, as well as the contractions. For the latter, flow direction is also of importance because not in every contraction, vena contracta effect is observed given in Figure 2.4. After the vena contracta, the fluid begins to recover pressure as the velocity decreases and the flow expands.

Results of the AMESim simulations are provided in Table 2.

Table 2 Parameters (left) and outputs (right) for all openings

Opening	Pressure/Flow Rate Inlet	Pressure Outlet	Orifice Area	Reynolds Number	Discharge Coefficient	Volumetric Flow Rate/Inlet Pressure
5 mm	315 bar	5 bar	34.87 mm^2	$1.23 * 10^6$	0.9	471.65 L/min
10 mm	315 bar	5 bar	139.6 mm^2	$1.23 * 10^6$	0.9	1888.24 L/min
20 mm	2500 L/min	5 bar	354.7 mm^2	643491	0.9	89.64 bar

40 mm	2500 L/min	5 bar	1256.64 mm^2	181659	0.9	11.76 bar

2.2 Geometry

The fluid domain is introduced, together with the components of the valves. All the technical drawings are provided by HTS, S.r.l. Fluid domain is created by the "volume extract" feature of Fluent. Since the domain is symmetric in the y-axis as seen in Figure 2.5, to reduce the computational effort, half of the geometry has been used as the domain for both valves. The simulations are done in a three-dimensional domain due to the geometry not being suitable for a two-dimensional domain. The inlet and outlet sections are compensated for development of flow and prevention of backflow respectively.

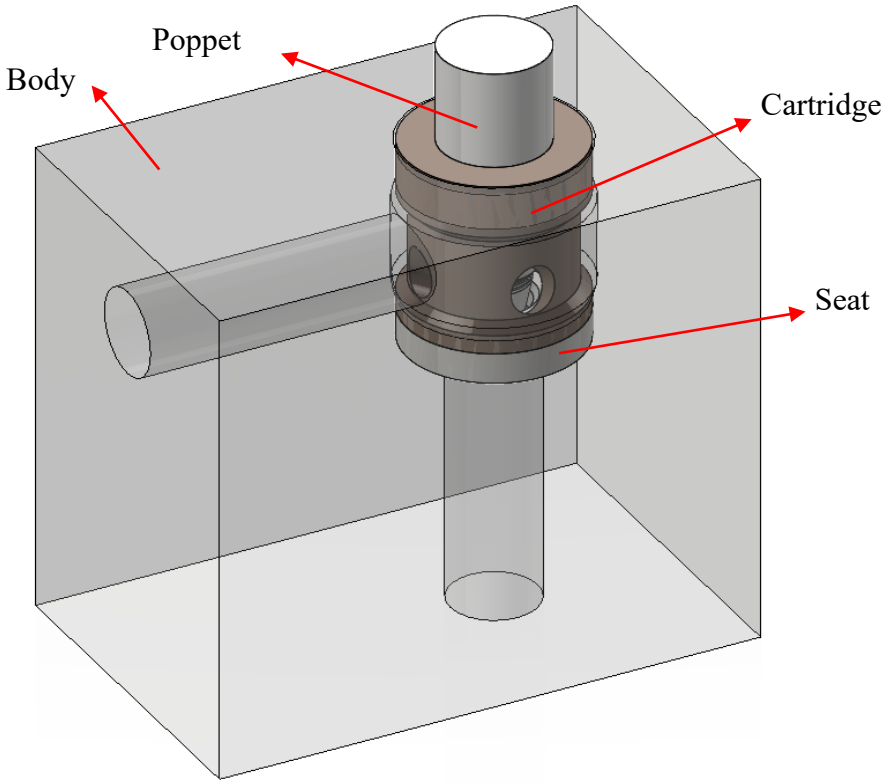

Figure 2.5 Three-dimensional fluid domain and commercial valve components

2.2.1 Commercial valve

Commercial valve consists of a cartridge with four holes to direct the flow after passing through the minimum area, that is between the poppet and the seat. The seat has a conical shape, to match the shape of the poppet when in contact. The body completes the assembly and includes the inlet and outlet of the system, shown in Figure 2.6.

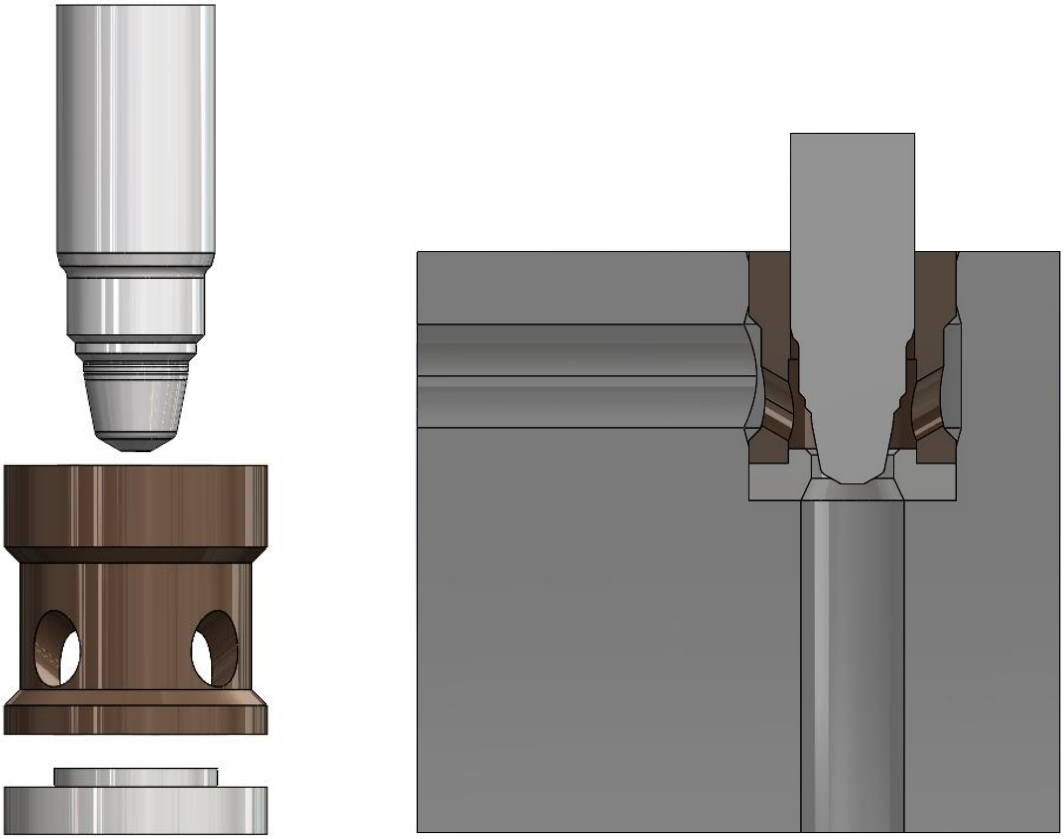

Figure 2.6 Commercial valve components (from top to bottom): poppet, cartridge and seat (left) and domain (right)

2.2.2 Prototype valve

Prototype valve differs from the commercial valve in terms of its cartridge and poppet. The cartridge is developed to create a secondary restricted section (along with the zone between the poppet and the seat) with the help of its many small holes, to induce a gradual pressure drop across the valve as studied in [6]. The poppet and the cage shown in Figure 2.7 is not the actual one used in this study but rather a similar model, provided for privacy reasons. In addition, the perforated cage helps transport the cavitation away from the valve body and to the cartridge itself. The cartridge can be easily substituted by a new one, however if the valve components are damaged, it is much more costly to substitute the entire valve, since both poppet and seat would be damaged. The fluid domains of commercial and prototype valve are given in Figure 2.8.

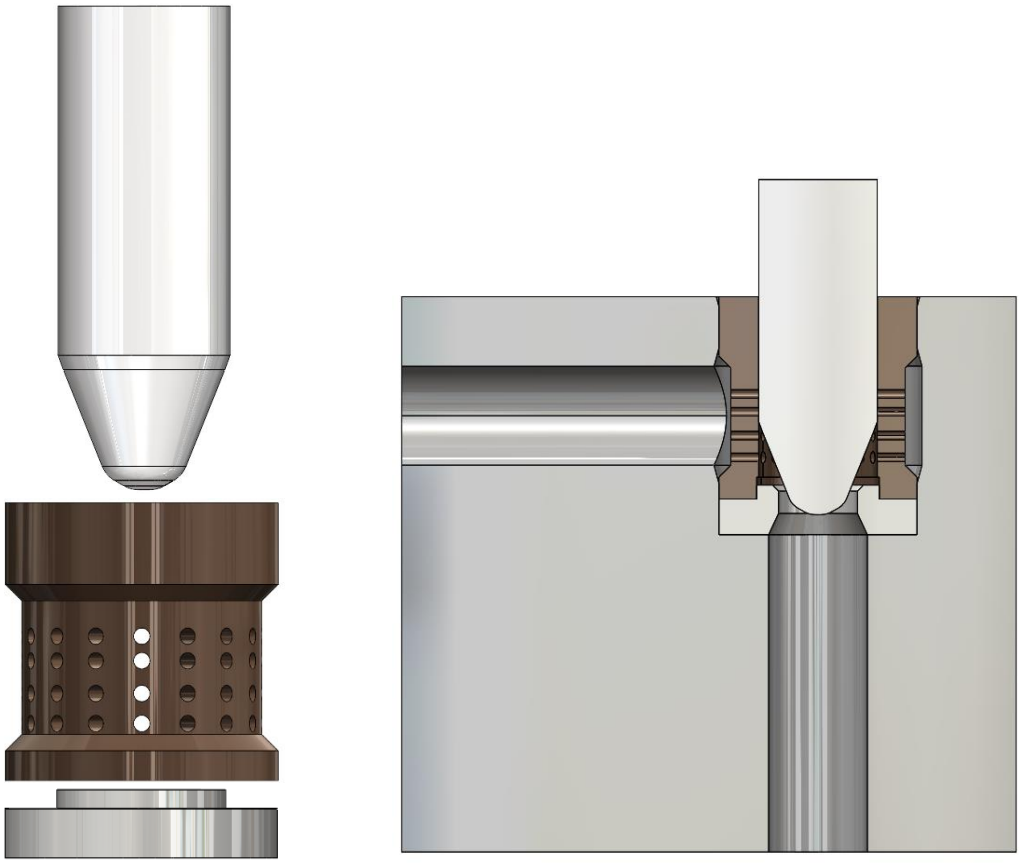

Figure 2.7 Prototype valve components (from top to bottom): poppet, cartridge and seat (left) and domain (right)

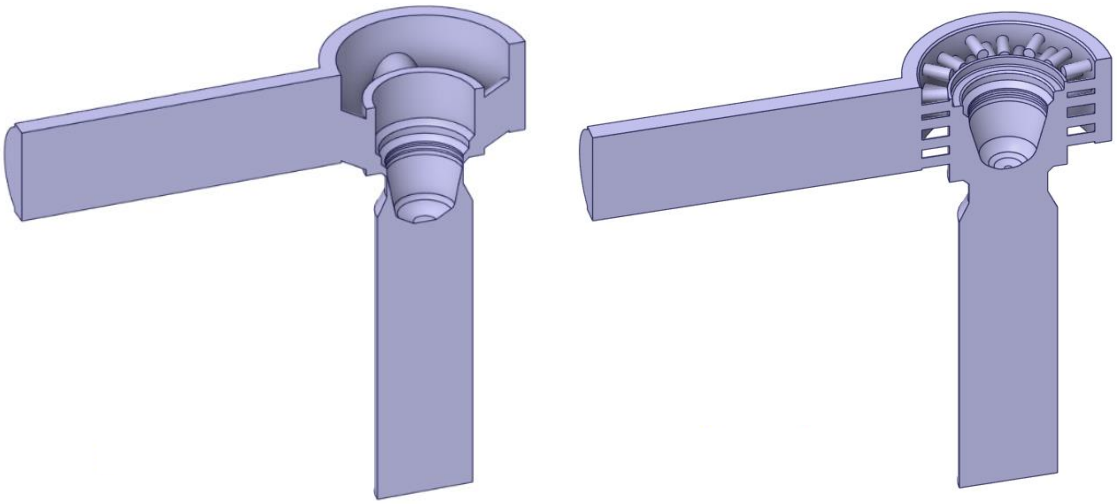

Figure 2.8 Simplified fluid domains: commercial valve (left), prototype valve (right)

2.3 Mesh

Correct discretization of the domain is of fundamental importance for obtaining an accurate solution. Mesh quality is a trade-off between solution accuracy, convergence rate and computational resources and time available to the user. Before meshing, the sections that are critical to the flow must be determined, so that specific settings may be applied to make sure that the resolution is done correctly. Such sections when simulating a valve flow can be named as the restricted flow passage area between the poppet and the seat and the section downstream, in case of a vena contracta effect is observed. In addition, early sections of the outlet can be considered, in case of an extension of cavitation to the said area. These zones can be decided by theoretical knowledge, but also together with a simulation of the problem. Mesh type is also important for accuracy and most importantly for computational time, given in Figure 2.9 for both two-dimensional and three-dimensional domains. Three mesh types have been investigated searching for the most convenient discretization: tetrahedral, sweep-hexagonal, and polygonal mesh.

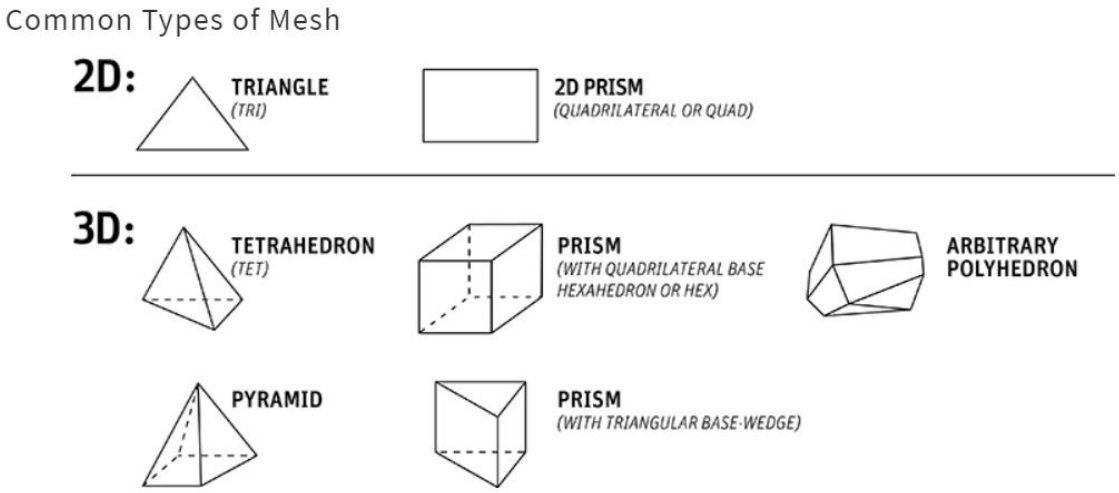

Figure 2.9 Common types of mesh (SimuTech Group)

Tetrahedral mesh consists of four-sided pyramidal elements that are very flexible in discretization. They are frequently used for complex domains for their ease of conformity and unstructured nature. However, in some cases they might present numerical inaccuracies and are not recommended where high precision is desired. In addition, tetrahedral mesh is created with a large number of elements leading to an increase in computational cost and memory usage. In Figure 2.10, an example of a tetrahedral mesh created for this study is provided.

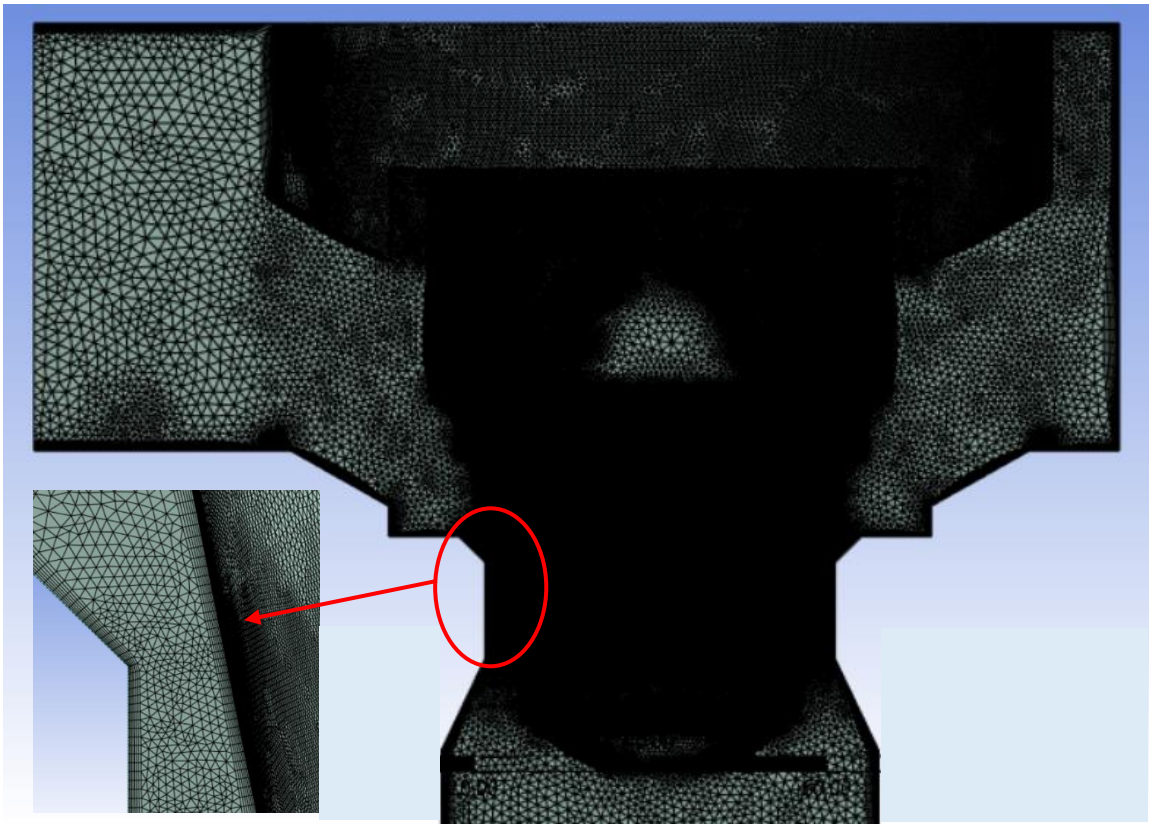

Figure 2.10 Tetrahedral mesh in commercial valve with emphasis on the throat (bottom left)

Hexagonal mesh is a structured mesh that is made of 3D hexagonal cells. Due to its regular nature, it is not adapted to resolving irregular geometries, creating problems of conformity. It provides high accuracy and less numerical diffusion if the flow is aligned with the mesh. This only happens in simple flows such as flow along a long straight duct. In such case, hexahedral mesh provides a better solution with fewer cells with respect to tetrahedral mesh. Hexahedral mesh is created using the sweep method that is created by sweeping the mesh pattern on a face of the domain through a path that naturally exists in the geometry. It is a fast and convenient way to create a mesh of excellent quality. However, it is preferrable that the path used for sweeping is also the path that is followed by the fluid flow. Otherwise, this method loses the advantage of its solution speed and therefore becomes inconvenient. In this mesh, the cartridge zone is meshed using tetrahedral elements due to its complex

geometry. A hexagonal mesh example that is abandoned for this study is depicted below in Figure 2.11.

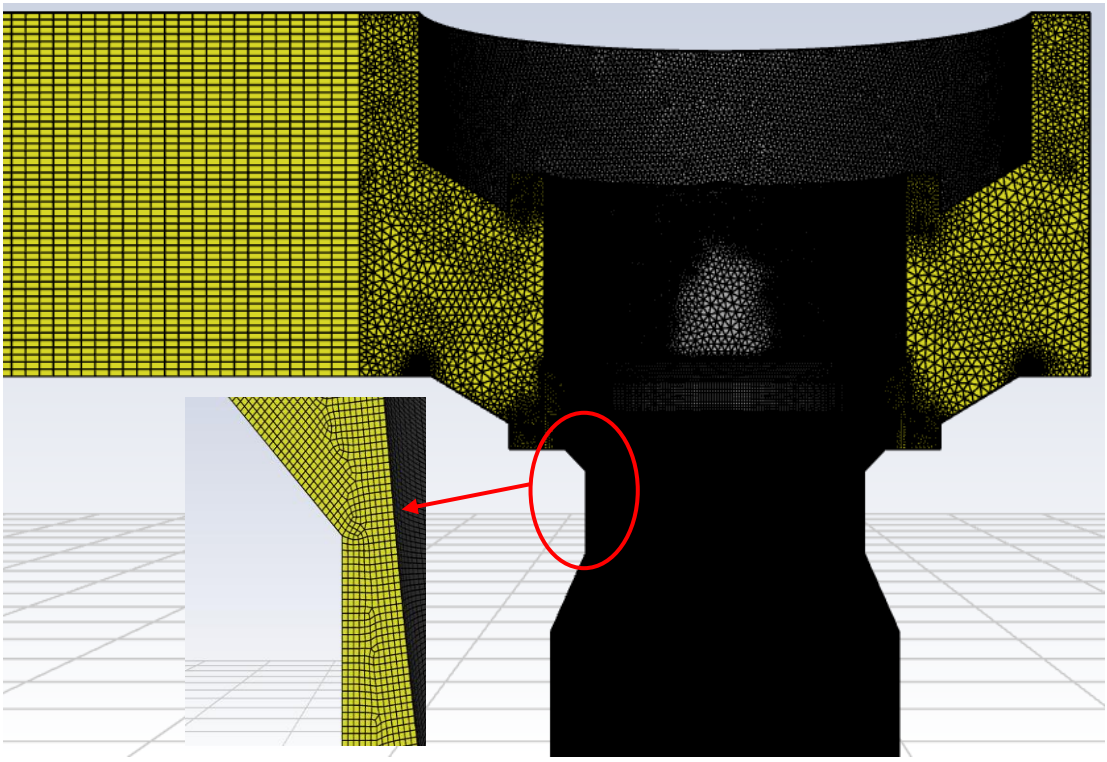

Figure 2.11 Tetrahedral mesh in commercial valve with emphasis on the throat (bottom left)

Polyhedral mesh is made up of elements that have many faces. This type of mesh can only be created from the Fluent Setup and the operation cannot be reversed. Polyhedral mesh reduces the cell number of the original tetrahedral mesh, saving computational resources by sacrificing the quality a negligible amount, and resulting in a much faster convergence. Although it occupies a significant amount of memory. One of the definitive polyhedral mesh used in this study is shown in Figure 2.12.

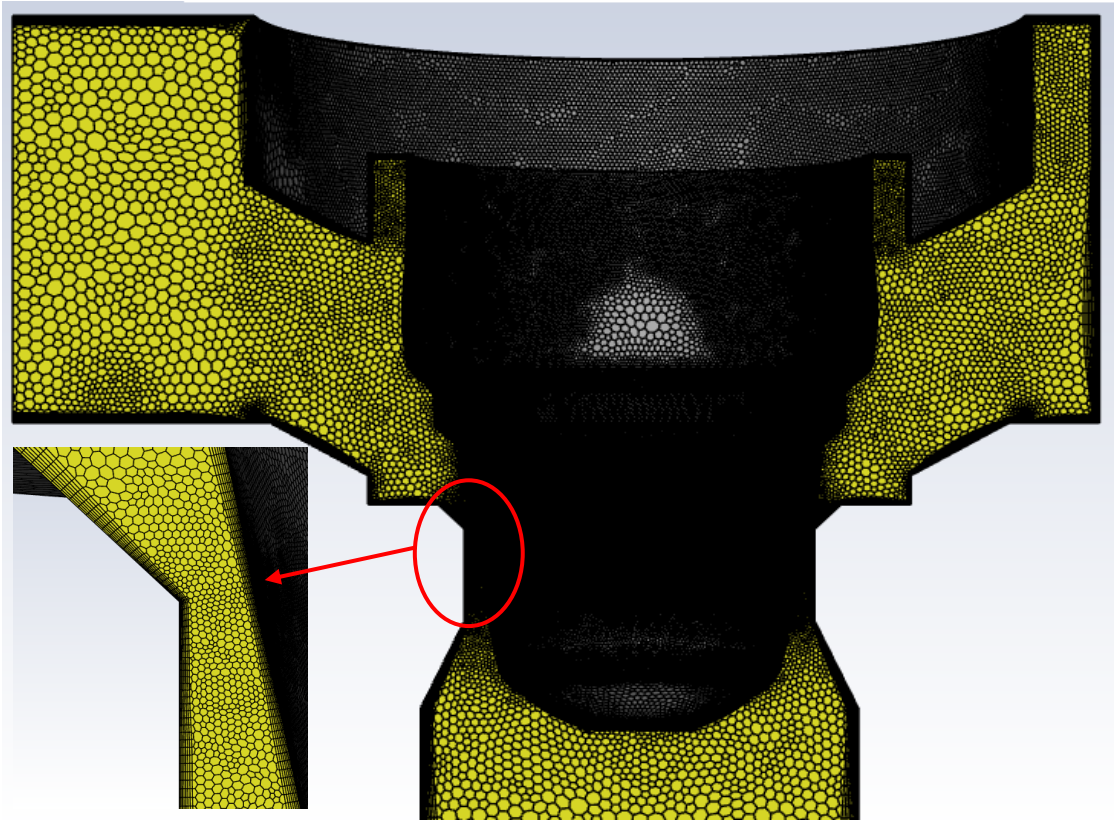

Figure 2.12 Polyhedral mesh in commercial valve with emphasis on the conical zone (bottom left)

The mesh can be evaluated through mainly three quality indicators: orthogonal quality, aspect ratio and skewness. If the mesh is not within the correct range of such indicators, it may result in bad physics description and illogical outputs in poor quality cells. It is also required to make sure that the solution is mesh independent, meaning that the solution output parameters should not change significantly when the mesh size changes. Thus, the correct number of cells should be found that gives the independent solution with the least cells. Mesh independence study will be discussed later.

Orthogonal quality is linked to the mesh cell under analysis and its neighbor cells. It is a measure of their cell centers' orientation with respect to each other. Mathematically, it is the minimum of $\frac{A_i \cdot f_i}{|\vec{A_i}||\vec{f_i}|}, \frac{A_i \cdot c_i}{|\vec{A_i}||\vec{c_i}|}$ for each face, i of a cell. Where A_i is the face normal vector, f_i is a vector from the cell center of the main cell to the centroid of the corresponding face and c_i is a vector from the cell center of the main cell to the cell center of the adjacent corresponding cell, as shown in Figure 2.13. Orthogonal quality can be anywhere between 0 and 1: 0 is the worst and 1 is the best cell.

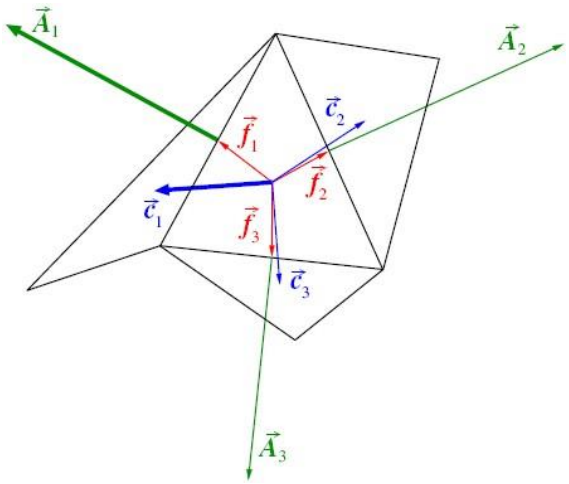

Figure 2.13 Orthogonal quality representation (Seeni, 2020)

Skewness is another mesh metric that is a measure of how equilateral the faces of a cell are. There are two methods when calculating skewness:

- Equilateral volume deviation: $Skewness = \frac{Optimal\ cell\ size - Cell\ Size}{Optimal\ cell\ size}$ (3)
- Normalized angle deviation: $Skewness = \max\left(\frac{\theta_{max} - \theta_e}{180 - \theta_e}, \frac{\theta_e - \theta_{min}}{\theta_e}\right)$ (4)

Where θ_e is the equiangular face/cell. Skewness is also between 0 (best) and 1 (worst). Representation of skewness is provided in Figure 2.14.

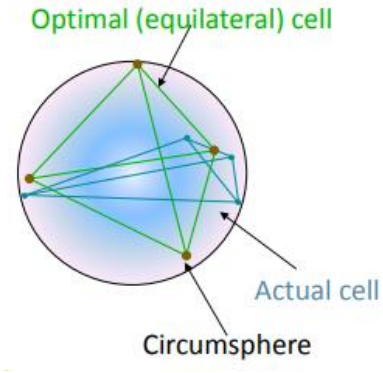

Figure 2.14 Skewness representation (ANSYS)

Aspect ratio is the ratio of the longest edge of the cell to its shortest edge. Starting from 1 it may take any value depending on the cell geometry. Examples on how to calculate the aspect ratio for common shapes are provided in Figure 2.15.

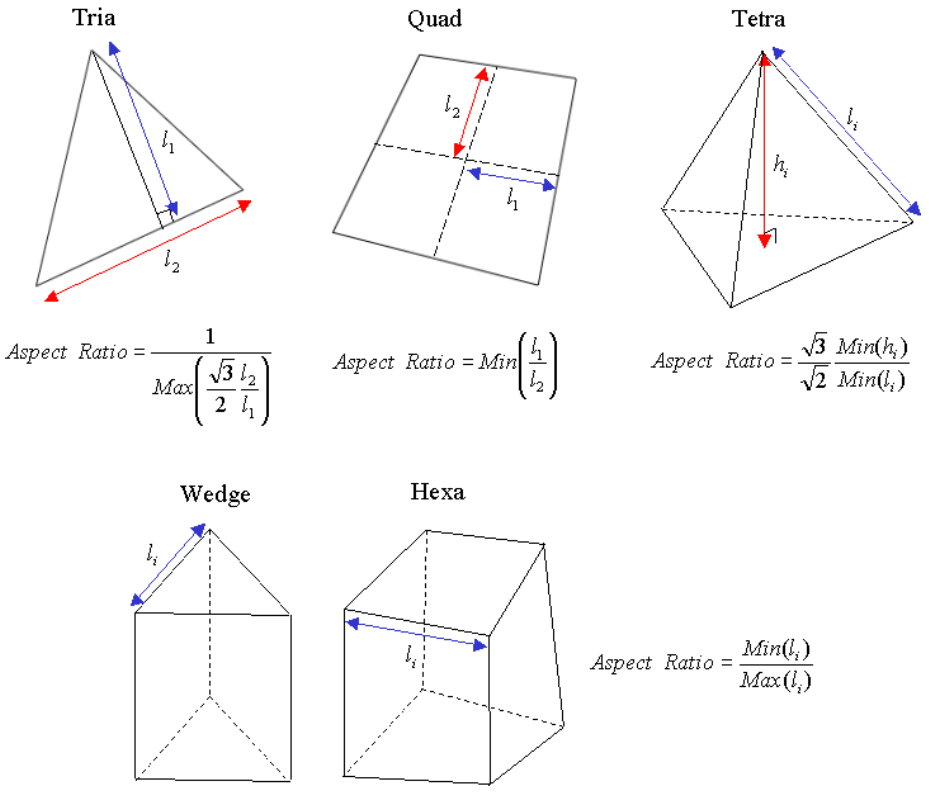

Figure 2.15 Aspect ratios for different shapes (Midas Geotechnical)

For an acceptable quality of mesh, the following criteria must be considered:

- $Orthogonal\ quality > 0.1$
- $Skewness < 0.95$
- $Aspect\ ratio < 120$

All the mesh created for this study falls in the presented range of quality measures. Quality measures of sample mesh are provided in Table 3.

Table 3 Quality measures of 10-millimeter opening converging flow commercial valve

Number of elements	Number of elements in restricted section	Orthogonal quality	Aspect ratio
6,336,099	19	0.34	39.08

2.3.1 Near-wall treatment

Boundary layer is formed whenever the fluid encounters a no slip wall. The velocity of the fluid is zero at the no-slip wall and increases moving away from the wall to the free stream velocity. The form of the boundary layer depends on the flow regime: laminar or turbulent, as seen in Figure 2.16, where U_0 is the free stream velocity, δ is the boundary layer thickness and y is the vertical distance from the wall. Passing from laminar to turbulent flow, a transition region is observed.

Such transition usually occurs at a Reynolds number $Re = 5 * 10^5$ for external flows, and at $Re = 2300$ for internal flows. Reynolds number is a dimensionless number that represents the ratio of inertial forces to viscous forces, given in Equation (5), where ρ is the fluid density, u is the flow speed, D is the characteristic diameter and μ is the dynamic viscosity of the fluid. Above these Reynolds numbers the flow is considered fully turbulent

and shows chaotic, irregular motion. Turbulence imposes increased mixing and diffusion with the help of small swirling structures called “eddies”.

$$Reynolds\ number, Re = \frac{\rho u D}{\mu} \quad (5)$$

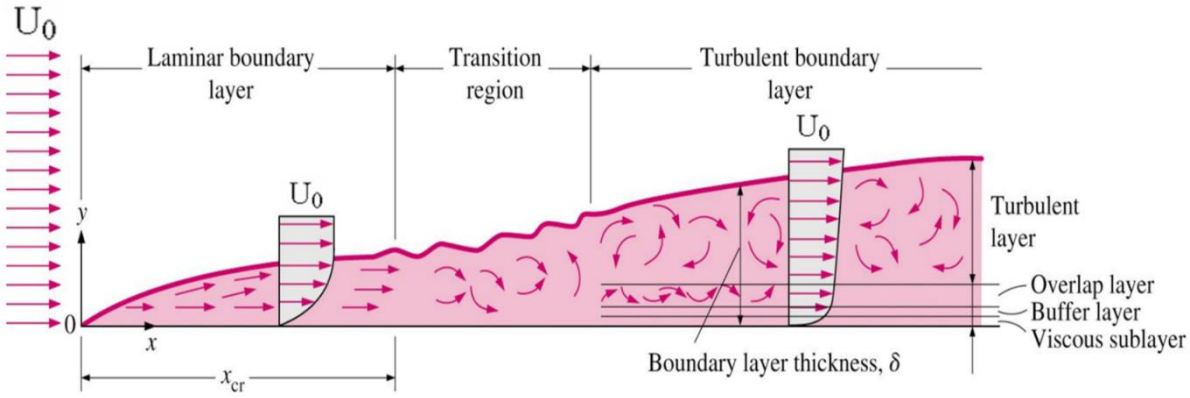

Figure 2.16 Boundary layer in different flow regimes (Cengel, 2018)

Near-wall modeling is essential to achieving accurate numerical solutions because walls are primary sources of vorticity and turbulence. In the near-wall region, solution variables exhibit steep gradients, and both momentum and scalar transport are at intense levels. Therefore, capturing the flow dynamics accurately in this region is crucial for reliable predictions of turbulent flows along walls. In this study the turbulent boundary layer will be considered since turbulent flow is expected with the given boundary conditions.

The most important parameter to consider when simulating a turbulent flow is the y-plus (y^+) value. y^+ is a non-dimensional parameter to calculate the first layer thickness of a mesh from the wall to correctly capture the boundary layer. Turbulent boundary layer consists of two main layers that are the inner and outer layers, and three layers inside the inner layer that are viscous sublayer, buffer layer and log-law layer (overlap layer), given in Figure 2.17. Thus, y^+ value depends on which sublayer in the turbulent boundary layer is wanted to be captured. In some flows, effects near the wall are required to be resolved, thus the viscous sublayer, that results in a computationally heavy mesh, since the first layer is extremely thin, for example, in a flow where the drag force is of interest. In other

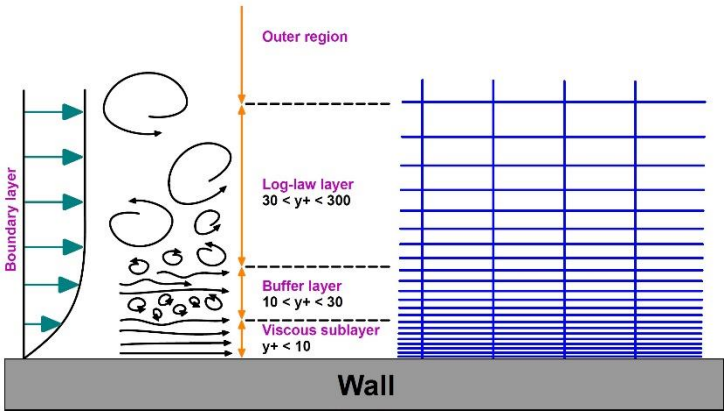

Figure 2.17 Y-plus intervals over the layers of the boundary layer (Khamlaj)

problems, where the wall effects are negligible, semi-empirical formulae can be used to pass from viscous sublayer to the fully turbulent region, which requires a computationally lighter mesh. y^+ is calculated as follows:

- Dimensionless wall distance: $y^+ = \frac{y u_\tau}{\nu}$ (6)
- Friction velocity: $u_\tau = \sqrt{\frac{\tau_w}{\rho}}$ (7)
- Wall shear stress: $\tau_w = \frac{1}{2} C_f \rho U_f^2$ (8)
- Skin friction coefficient: $C_f = \frac{0.026}{Re^{\frac{1}{7}}}$ (9)
- Dimensionless velocity: $u^+ = \frac{u}{u_\tau}$ (10)

Where y is is the dimensionless wall distance, ρ is the fluid density, U_f is the free stream velocity, and u is the local velocity in the boundary layer.

To be noted that, depending on the value of y+, the location of the first layer of the mesh changes such that:

- If y+<5, the first grid cell is in the viscous sublayer.
- If 5<y+<30, the first grid cell is in the buffer layer.
- If 30<y+<300, the first grid cell is in the log-law layer.

Viscous sublayer

The viscous sublayer is a very thin layer closest to the no-slip wall where viscous shear is much greater than turbulent shear stress. The eddies close to a smooth solid surface are damped since the fluid velocity is zero at the wall, $u = v = w = 0$, resulting in a laminar flow in this layer. Here, the viscous shear is almost equal to wall shear stress τ_w.

$$\tau_y = \mu \frac{\partial U}{\partial y} \approx \tau_w \tag{11}$$

Thus, applying the boundary conditions, a linear relationship is obtained:

$$u^+ = y^+ \tag{12}$$

Log-law region

In the log-law layer, turbulent mixing dominates over viscous effects. Wall functions that are used in CFD codes exploit log-law equation to model flow behavior near the wall to reduce the necessity to use computationally heavy meshes. Dimensionless velocity correlates with dimensionless wall distance as:

$$u^+ = \frac{1}{\kappa} ln y^+ + B \tag{13}$$

Where κ is the von Karman constant, around 0.41 and B is an empirical constant around 5.

Buffer layer

The buffer layer serves as a transitional layer between the viscous sublayer and the log-law region where both viscous and turbulent shear stress are significant. There is no equation that satisfies the relationship between y^+ and u^+ as seen in Figure 2.18. This is a critical region to fall into, since the velocity profile is not well-defined, it is best practice to avoid this region when choosing the height of the first cell.

Hence, for the near-wall treatment for the two valves, “inflation (as called in ANSYS Fluent)” is added to the mesh to capture the boundary layer, and eventually obtain a more accurate result. The first layer thickness is calculated for each case using Equations (6,7,8,9,10).

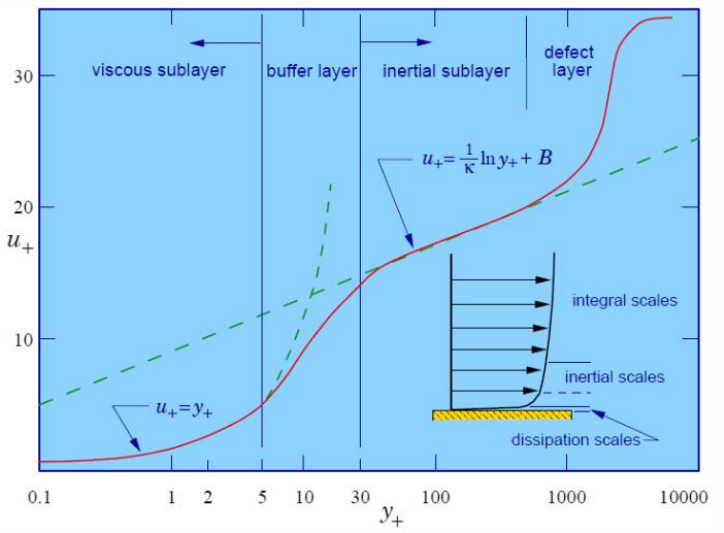

Figure 2.18 Dimensionless velocity versus dimensionless wall distance (LearnCax)

Flow models such as Spalart-Allmaras and k-omega are already suitable to be applied throughout the boundary layer, if the mesh near the walls is fine enough. On the other hand, models such as k-epsilon and Large Eddy Simulation (LES) are more accurate for simulating turbulent core flows: regions that are farther from walls. Hence, to make these

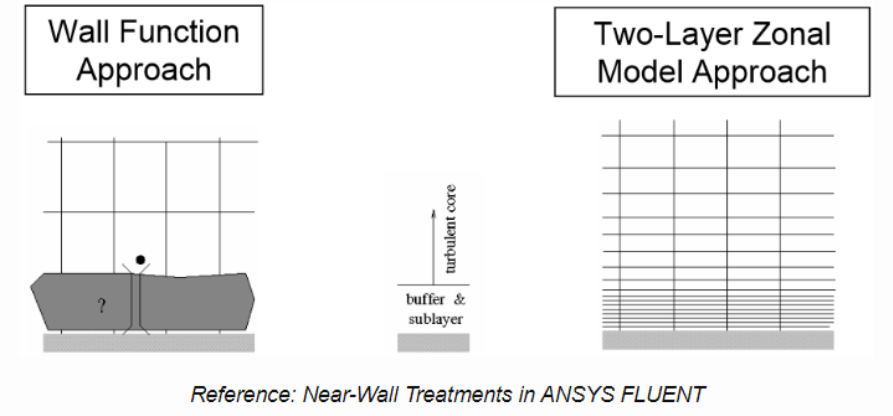

Figure 2.19 First cell sizes for wall function and two-layer zonal approach (ANSYS)

models effective for flows near wall boundaries, further adjustments are necessary, that are called wall functions. Near-wall treatment techniques used in ANSYS are shown in Figure 2.19.

Wall functions save computational time and effort by eliminating the need for resolving the viscous sublayer, instead, empirical relationships are applied to estimate the solution variables without sacrificing the accuracy of the solution. The first cell from the wall is assumed to fall inside the log-law layer. Wall functions are used especially for high-Reynolds-number flows.

Calculation of the wall y^+ is not straightforward for this study, since velocity information is not provided for the inlet. Therefore, the discharge coefficient should be assigned a nominal value to approximate the inlet velocity. In the end, y^+ should be in a certain interval instead of an exact value and thus an approximation works well.

Table 4 Wall distance calculation results

Free-stream velocity [m/s]	13	
Density [kg/m3]	998.2	
Dynamic viscosity [kg/m s]	1e-3	
Boundary layer length [m]	0.05	
Reynolds number [-]	650000	
Desired y^+ value [-]	1	100
Estimated wall distance [m]	1.7e-6	1.7e-4

Wall distance calculation results are given in Table 4. According to the results, $y^+ = 100$ should be aimed for since $y^+ = 1$ requires extremely small inflation layers that will create quality problems.

2.3.2 Mesh independence study

Mesh independence study must be done to ensure that the solution obtained is independent of the discretization of the domain. The solution accuracy and convergence improves as the grid is refined, such as in DNS method that provides the most accurate solution, the grid is created with extremely small elements to perfectly capture the flow dynamics. In addition, a coarse mesh can result in unphysical phenomena and numerical instabilities, that does not correspond to the real behavior of the system. Mostly, the results of the mesh independence study are compared to an analytical or experimental benchmark. In this study, where experimental data is unavailable, the results of the mesh independence study are compared to one another to assess whether any significant changes occur.

The case of maximum opening of the commercial valve has been selected for the grid independence test, as it represents the scenario with the least expected cavitation. This ensures that the quantitative nature of the grid independence study is not influenced by the single-phase solution, which is used in the context of a multiphase problem.

The grid is refined mainly around the zone where poppet and seat are located while the variation of the inlet pressure value is investigated. The rest of the parameters are kept unchanged. The results of the mesh independence are given below in Table 5.

Table 5 Mesh independence results

Number of Elements	Element Size at the Throat	Inlet Pressure
$6.3 * 10^6$	0.4	17.89
$7.9 * 10^6$	0.18	17.72
$9.2 * 10^6$	0.15	17.54

It is observed that the difference between the results is approximately 1%, with a decreasing trend. Since the results do not exhibit significant variation, the intermediate case is selected for further investigation in the CFD analysis.

2.4 Setup

In this section the setup process of the fluid-dynamic problem is presented. As stated before, half of the geometry is used due to the domain being symmetric in YZ plane and the boundary conditions are accounted for accordingly. In total, 12 single-phase simulations are done for two valve geometries, two flow types and four openings, shown in Table 6 together with their corresponding names to facilitate referencing throughout the text. Maximum valve opening is 40 millimeters. Simulations for 5- and 10-millimeter openings investigate the flow rate passing from the restricted area using pressure inlet boundary condition. 20- and 40-millimeter opening simulations are done to evaluate the inlet pressure level, with mass flow rate as an input at the inlet. In this study, single-phase approach is preferred due to the large number of simulations to be completed since multiphase model requires more computational time to achieve convergence. When studying the cavitation phenomena in a single-phase flow simulation, zones with pressure under the vapor pressure of the working fluid must be investigated. This approach is not problematic for the current study, as it adopts a comparative framework. Hence, a single-phase simulation can give a vast idea about the performance of the prototype valve in terms of cavitation reduction, with respect to the commercial valve. Although, a multiphase simulation is done just for C-C10 case to identify the distinctions between the two approaches, and to obtain a definitive flow rate, as stated in [9], single phase simulations where cavitation is observed tend to overpredict the flow rate. Multiphase option is enabled on top of the converged single-phase simulation as suggested in [10]. Moreover, a new valve body proposed by HTS S.r.l. in case of a cavitation extension to the outlet section of the valve, is analyzed for the cases where such a problem is observed.

Table 6 Simulations done for the study with corresponding names

		Opening [mm]			
Valve Type	**Flow Type**	**5**	**10**	**20**	**40**
Commercial	Converging	C-C5	C-C10	C-C20	C-C40
	Diverging	C-D5	C-D10		
Prototype	Converging	P-C5	P-C10	P-C20	P-C40
	Diverging	P-D5	P-D10		

The working fluid is water at 25°C. Pressure-based solver is preferred due to the incompressible nature of the flow. Realizable k-ε model with enhanced wall treatment as the wall function is selected. For the turbulent viscosity, 5% that is the default value is left as there is no specific information about the problem for this setting. In addition, hydraulic diameter was chosen as the second setting for turbulence, and the inlet diameter of 50 millimeters is provided. For pressure-velocity coupling, coupled solver is preferred to the segregated solver because it performs better in single-phase steady-state flows, although it does not work well with multiphase flows. The coupled algorithm simultaneously solves the momentum equations and the pressure-based continuity equation. Full implicit coupling is achieved by applying an implicit discretization to the pressure gradient terms in the momentum equations, as well as to the mass flux across faces, which includes the Rhie-Chow pressure dissipation terms. Green-Gauss Node-Based approach is used for gradient evaluation since it is considered the most accurate approach, however, as in most cases it is computationally more expensive. In this approach, the face scalar is computed as the arithmetic average of the nodal values on the face:

$$\overline{\varphi_f} = \frac{1}{N_f}\sum_n^{N_f} \varphi_n \quad (14)$$

Where N_f corresponds to the number of nodes on the face. This method reconstructs the exact values of a linear function at a node based on the surrounding cell-centered values on arbitrary unstructured meshes by solving a constrained optimization problem, while maintaining second-order spatial accuracy. For the spatial discretization of momentum, turbulent kinetic energy and turbulent dissipation rate, first order accuracy is chosen for the initial solution. After convergence is obtained, all the variables are set to second order accuracy. Convergence criterion is set to when all the residuals fall below 10^{-4}. For the multiphase simulation, PRESTO is used for pressure-velocity coupling. The two phases are water-liquid and water-vapor. The default model of cavitation dynamics, Schnerr-Sauer, is selected. The domain is patched prior to the calculation, so that it is filled with liquid completely. This process is crucial for preventing the simulation from diverging, as high-pressure gradients in confined regions are anticipated, which can lead to instability. Table 7 is provided to summarize all the settings for the simulations.

Table 7 Settings for the CFD simulations

Settings	Parameter	Type	
Physical properties	Water-liquid	Density [kg/m^3]	998.2
		Viscosity [kg/m s]	1e-2
	Water-vapor	Density [kg/m^3]	5.54e-1
		Viscosity [kg/m s]	1.34e-05
Boundary conditions	Inlet boundary	Pressure inlet [bar]	315
		Mass flow inlet [kg/s]	20.79
	Outlet boundary	Pressure outlet [bar]	5
Computation model	Single-phase	Turbulence model	Realizable k-epsilon (EWT)
		Scheme	Coupled
		Gradient	Green-Gauss Node Based
		Pressure	2nd order upwind
		Momentum	2nd order upwind
		Turbulent kinetic energy	2nd order upwind
		Turbulent dissipation rate	2nd order upwind
	Multiphase	Cavitation model	Schnerr-Sauer

	Scheme	SIMPLE
	Vaporization pressure [bar]	3.54e-2

Boundary conditions are denoted as follows:

- Pressure inlet: $p_{inlet} = 315 \text{ bar}$ (15)
- Mass flow inlet: $\dot{m} = \rho U A = 41.58 \text{ kg/s}$ (16)
- Symmetry: $\frac{\partial \phi}{\partial n} = 0, \mathbf{v} \cdot \hat{n} = 0$ (17)
- Wall: $\frac{\partial \phi}{\partial n} = 0$ (adiabatic wall), $\mathbf{v} \cdot \hat{n} = 0, \mathbf{v} = 0$ (no − slip condition) (18)
- Pressure outlet: $p_{outlet} = 5 \text{ bar}$ (19)

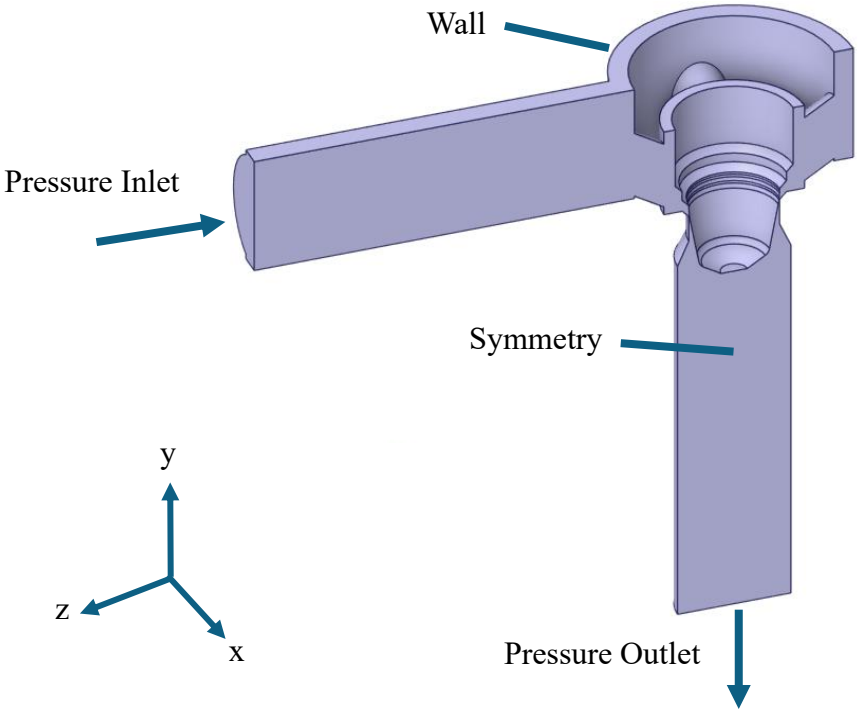

Figure 2.20 Boundary conditions for converging flow

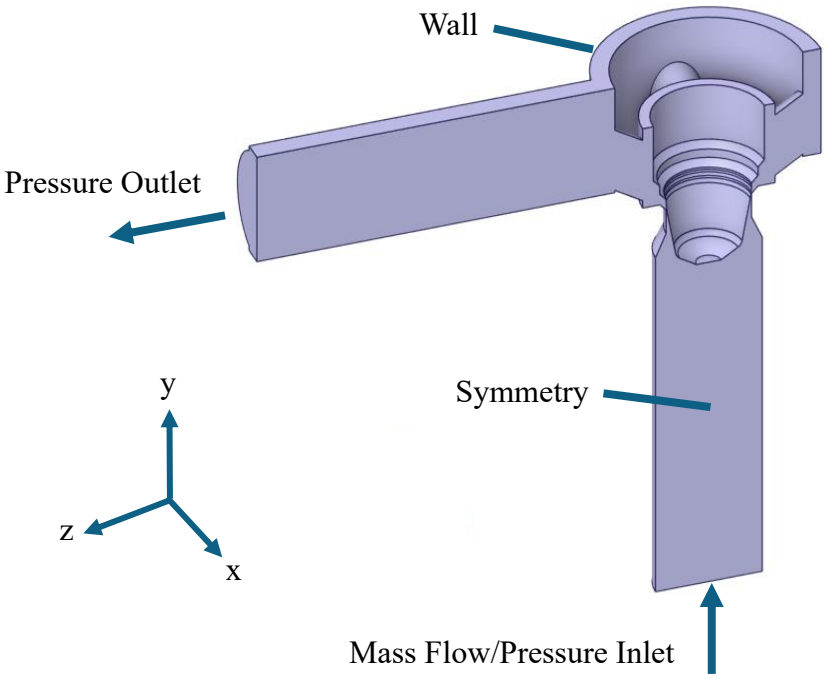

Figure 2.21 Boundary conditions for diverging flow

In Figures 2.20 and 2.21, the boundary conditions for converging and diverging flow are illustrated respectively. In converging flow, the fluid enters the domain in $-z$ direction and exits the domain in $-y$ direction meanwhile in diverging flow the entrance becomes the exit and vice versa. Symmetry boundary condition denotes that there is no normal velocity or flux throughout the boundary, so that the flow properties are mirrored on either side of the domain. ϕ represents any kind of field variable such as pressure, temperature or scalar quantities, where $\hat{n}$ is the unit normal to the boundary. Wall boundary condition is similar to the symmetry boundary condition, although no slip condition is added so that velocity of the fluid at the wall is equal to the velocity of the wall. Thus, if the wall is stationary, fluid velocity is zero. In addition, the effect of the moving poppet during the opening of the valve has been found insignificant to the velocity of the fluid in previous studies, since it is much smaller in magnitude. Thus, the poppet has been simulated stationarily [12].

2.4.1 Model of turbulence

Many turbulence models are implemented in Fluent software such as LES and RANS that employ modelling at some scale as the name suggests. The selection of the model depends on the computational resources and time available to the user and desired level of accuracy of the results. The most accurate solution can be obtained using DNS (Direct Numerical Solution), where all the length scales of turbulence are completely resolved using Navier-Stokes equations (20, 21) from the largest integral scale to the smallest Kolmogorov length scale. The Kolmogorov length scale includes the smallest eddies that are dissipated as heat. This approach requires an excellent mesh that is about the cube of the Reynolds number, and a very small time-step size. Thus, it is not used in industry but only in literature, to study non-complex problems such as flow around a sphere.

Continuity equation: $\nabla \cdot \mathbf{u} = 0$ (20)

Momentum equation: $\frac{\partial \mathbf{u}}{\partial t} + (\mathbf{u} \cdot \nabla)\mathbf{u} = -\frac{1}{\rho}\nabla p + \nu \nabla^2 u + \mathbf{f}$ (21)

Where $\mathbf{u} = (u, v, w)$ is the velocity field in three spatial coordinates x, y and z, t is time, p is the pressure, $\mathbf{f}$ is the external body force.

LES (Large Eddy Simulation) provides a middle way between full modelling and DNS. In this model, “large eddies” are resolved while dissipative small eddies are modelled, since resolving them requires a much larger computational resource. In addition, small eddies are seen to be isotropic, and they do not get influenced by the boundary conditions as much as large eddies do. At this point, a filtering process is applied to remove the eddies below the limit, that brings additional unknowns while manipulating the exact Navier-Stokes equations. LES is more accessible than DNS and may be used in both industry and for academic purposes, in aerodynamics in turbomachinery, automative industry and so on.

RANS (Reynolds-Averaged Navier Stokes) model is obtained by averaging the flow quantities that are resolved numerically while the fluctuations outside the mean quantity are

modelled. In this method, all the turbulent scales independent of size are modelled. In Figure 2.22, the comparison between the flow models is provided.

Velocity: $u_i = \overline{u_i} + u_i'$ (22)

Pressure and other scalars (energy, species concentration): $\varphi = \bar{\varphi} + \varphi'$ (23)

Substituting Equations (22, 23) into Equations (20, 21), it is obtained:

$$\frac{\partial \rho}{\partial t} + \frac{\partial}{\partial x_i}(\rho u_i) = 0 \quad (24)$$

$$\frac{\partial}{\partial t}(\rho u_i) + \frac{\partial}{\partial x_j}(\rho u_i u_j) = -\frac{\partial p}{\partial x_i} + \frac{\partial}{\partial x_j}\left[\mu\left(\frac{\partial u_i}{\partial x_j} + \frac{\partial u_j}{\partial x_i} - \frac{2}{3}\delta_{ij}\frac{\partial u_l}{\partial x_l}\right)\right] + \frac{\partial}{\partial x_j}\left(-\rho\overline{u_i' u_j'}\right) \quad (25)$$

The term $-\rho\overline{u_i' u_j'}$ in Equation (25) is denoted as Reynolds stresses and they represent the additional term in Navier-Stokes equations, which must be modelled.

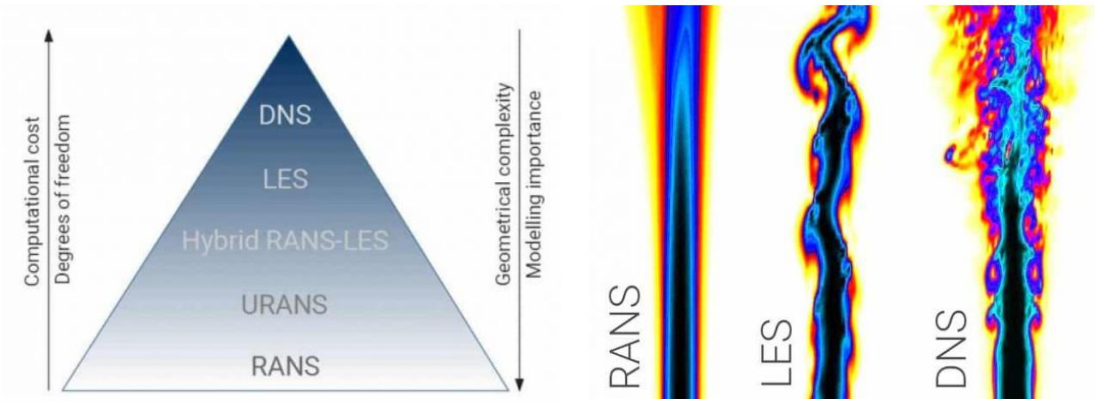

Figure 2.22 Comparison of turbulent flow models (Ideal Simulations)

RANS model is used in this solution considering the computational resources and number of simulations. RANS consists of mainly four models that are generally used in simulations: Standard $k-\omega$, SST $k-\omega$, Standard $k-\epsilon$, Realizable $k-\epsilon$ and RNG $k-\epsilon$.

Standard $k-\epsilon$ is used for high Reynolds number flows where fully turbulent flow conditions are observed. A constant turbulent Prandtl number and isotropy of turbulence are

assumed. It is a computationally cheap model with respect to others. Turbulent dissipation rate, ϵ is the main key variable for turbulent transport equations in this family.

Realizable $k-\varepsilon$ is an improved version of the standard $k-\varepsilon$ model. It is better in terms of capturing the turbulence effects especially in rotating flows and flows with high shear. It is mostly preferred over standard $k-\varepsilon$.

RNG $k-\varepsilon$ (Re-Normalization Group) brings re-normalization procedure to the standard $k-\varepsilon$ model to improve its accuracy in complex flows where strong pressure gradients are observed. All the $k-\varepsilon$ family models struggle to predict accurately the separation in flows.

Standard $k-\omega$ is more suitable for low Reynolds number flows and flows near walls, as it uses specific dissipation rate (ω) that is more sensitive to the boundary layer.

SST $k-\omega$ (Shear Stress Transport) is created to combine the strengths of both $k-\varepsilon$ and $k-\omega$ family. Thus, in near-wall region it uses $k-\omega$ model where $k-\varepsilon$ is less accurate and instead in free stream, it passes to $k-\varepsilon$ model. It offers good accuracy in separation flows and manages to simulate the turbulence well in the wake region although being computationally expensive particularly for large domains.

For this study, realizable $k-\varepsilon$ model is selected to conduct all the simulations. In [8], the three computationally inexpensive models of $k-\varepsilon$ family have been tested for a relief valve simulation and it has been found that there is no significant difference between the three for cavitation inception prediction. The equations used in realizable $k-\varepsilon$ model for turbulence kinetic energy, k and dissipation rate ϵ are as follows [2]:

$$\frac{\partial}{\partial t}(\rho k)+\frac{\partial}{\partial x_j}(\rho k u_j)=\frac{\partial}{\partial x_j}\left[\left(\mu+\frac{\mu_t}{\sigma_k}\right)\frac{\partial k}{\partial x_j}\right]+G_k+G_b-\rho\varepsilon-Y_M+S_k \tag{26}$$

$$\frac{\partial}{\partial t}(\rho \varepsilon)+\frac{\partial}{\partial x_j}(\rho \varepsilon u_j)=\frac{\partial}{\partial x_j}\left[\left(\mu+\frac{\mu_t}{\sigma_\varepsilon}\right)\frac{\partial \varepsilon}{\partial x_j}\right]+\rho C_1 S\varepsilon-\frac{\rho C_2 \varepsilon^2}{k+\sqrt{\nu\varepsilon}}+C_{1\varepsilon}\frac{\varepsilon}{k}C_{3\varepsilon}G_b+S_\varepsilon \tag{27}$$

Where $C_1=\max\left[0.43,\frac{\eta}{\eta+5}\right]$, $\eta=S\frac{k}{\varepsilon}$, $S=\sqrt{2S_{ij}S_{ij}}$, G_k is the generation of turbulence kinetic energy due to the main velocity gradients, G_b is the generation of turbulence kinetic

energy due to buoyancy and Y_M accounts for the contribution of the fluctuating dilatation in compressible turbulence to the overall dissipation rate. σ_k and σ_ε are the turbulent Prandtl numbers where σ_k=1 and $\sigma_\varepsilon = 1.2$ and S_k and S_ε are user-defined source terms for k and ε respectively. C_1, $C_2 = 1.9$ and $C_{1\varepsilon} = 1.44$ are constants. Turbulent viscosity μ_t is given as:

$$\mu_t = \rho C_\mu \frac{k^2}{\varepsilon} \tag{28}$$

Where $C_\mu = 0.09$ is a constant.

2.4.2 Model of cavitation

Cavitating flows are highly sensitive to the creation and movement of vapor bubbles, the fluctuations in pressure and velocity caused by turbulence, and the amount of non-condensable gases that are dissolved or introduced into the liquid during operation. There are mainly two models for multiphase flows in Ansys Fluent namely volume of fluid and mixture. The two models differ in terms of the assumptions made, computational requirements and levels of accuracy. In this study mixture model is utilized since volume of fluid method would be too heavy computationally for a three-dimensional problem. Fundamental theoretical studies of cavitation focus on the dynamics of bubbles (or bubble clouds) by solving for the vapor-liquid interface, while most practical cavitating flows are analyzed using homogeneous flow theory. This approach treats the fluid as a single substance with variable density, without explicitly considering phase interfaces. The development of this model followed a thorough review of experimental data, and an assessment of the computational costs associated with simulating cavitating flows where various Reynolds Averaged Navier-Stokes (RANS) solvers have been adapted to incorporate the dynamics of the secondary phase, including vapor and gas behavior. All phases share the common mixture velocity. In the mixture model, two cavitation models are proposed: Schnerr-Sauer and Zwart-Gerber-Belamri. The default model of Schnerr-Sauer has been selected of which the equations are presented below.

$$\rho_m = \alpha\rho_v + (1-\alpha)\rho_l \tag{29}$$

$$\alpha = \frac{Vol_{vapor}}{Vol_{liquid}+Vol_{vapor}} \tag{30}$$

$$\frac{\partial \rho_m}{\partial t} + \rho_m \nabla \cdot u_m = R_e - R_c \tag{31}$$

$$\rho_m = (1-\alpha)\rho_l + \alpha\rho_v \tag{32}$$

$$\mu_m = (1-\alpha)\mu_l + \alpha\mu_v \tag{33}$$

Where α is the vapor volume fraction and liquid phase is denoted by $\alpha = 0$ while $\alpha = 1$ denotes complete vapor. Vapor volume fraction brings an additional unknown to the problem. Equations (31, 36) are the continuity and momentum equations respectively, rewritten for the mixture phase that is denoted by the subscript m. In addition, ρ_m and μ_m denote the density and viscosity of the mixture respectively, the subscript l corresponds to liquid while v to the vapor phase. R_e and R_c are mass transfer source terms representing the growth and collapse of vapor bubbles respectively.

When $p_v > p$, denoting the condition for vapor bubbles to form:

$$R_e = \frac{\rho_v \rho_l}{\rho} \alpha(1-\alpha) \frac{3}{R_B} \sqrt{\frac{2}{3}\frac{(p_v - p)}{\rho_l}} \tag{34}$$

Instead, if $p > p_v$, the formed bubbles collapse, having travelled to a zone with higher pressure:

$$R_c = \frac{\rho_v \rho_l}{\rho} \alpha(1-\alpha) \frac{3}{R_B} \sqrt{\frac{2}{3}\frac{(p - p_v)}{\rho_l}} \tag{35}$$

$$\frac{\partial}{\partial t}(\rho_m \vec{u}) + \nabla(\rho_m \vec{u}\vec{u}) = -\nabla p + \nabla[\mu_m(\nabla\vec{u} + \nabla\vec{u}^T)] + \rho_m \vec{g} + \vec{F} \tag{36}$$

3 Results

In this section, the results of the CFD simulations are presented and discussed. Necessary comparisons are provided for a better evaluation of the cavitation characteristics.

3.1 Analysis of cavitation of the commercial valve

For a first analysis of cavitation, the C-D10 case is investigated. Static pressure throughout the valve is given in Figure 3.1.

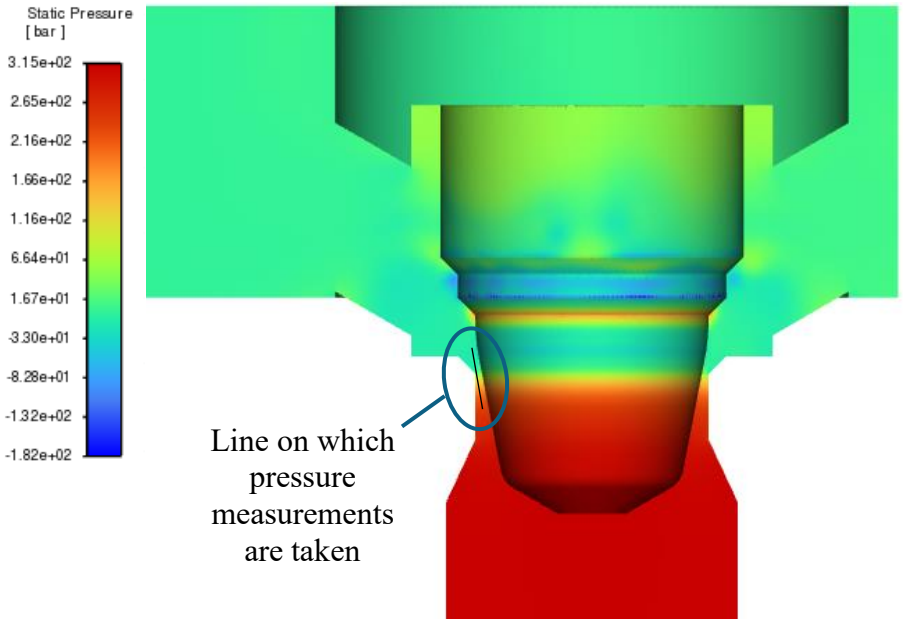

Figure 3.1 Static pressure contour of C-D10

As expected, a pressure drop, as a consequence of an increase in fluid velocity due to the decreasing flow area, is observed through the restricted section according to Bernoulli's principle. Flow rate across the valve is characterized by this restricted zone between the poppet and the seat, which corresponds to the minimum area where the fluid flows. Moving far away from the conical area, it is seen that pressure recovers a little through the outlet section. It has also been observed that negative pressure zones occur in certain areas of the valve, which do not correspond to a physical result. This is a consequence of using single-phase flow simulation instead of a multiphase model where cavitation could be simulated.

In a real-life flow, pressure cannot go below that of the vapor pressure of the fluid, so that it remains constant downstream of the orifice where such pressure is reached. Vapor bubbles that are formed induce choking phenomena, resulting in the flow rate remaining constant throughout the remaining valve section. However, this is not the case, shown in Figure 3.2 where static pressure is given as a function of the height of a line that goes through the restricted area of the valve (black line in Figure 3.1). The direction of the valve is in accordance with the flow direction. The pressure drops suddenly at a small length, and it is possible to see the recovery through the end where the pressure goes above the dashed line. The dashed line can be associated with cavitation, that below it vapor bubbles can be expected to form.

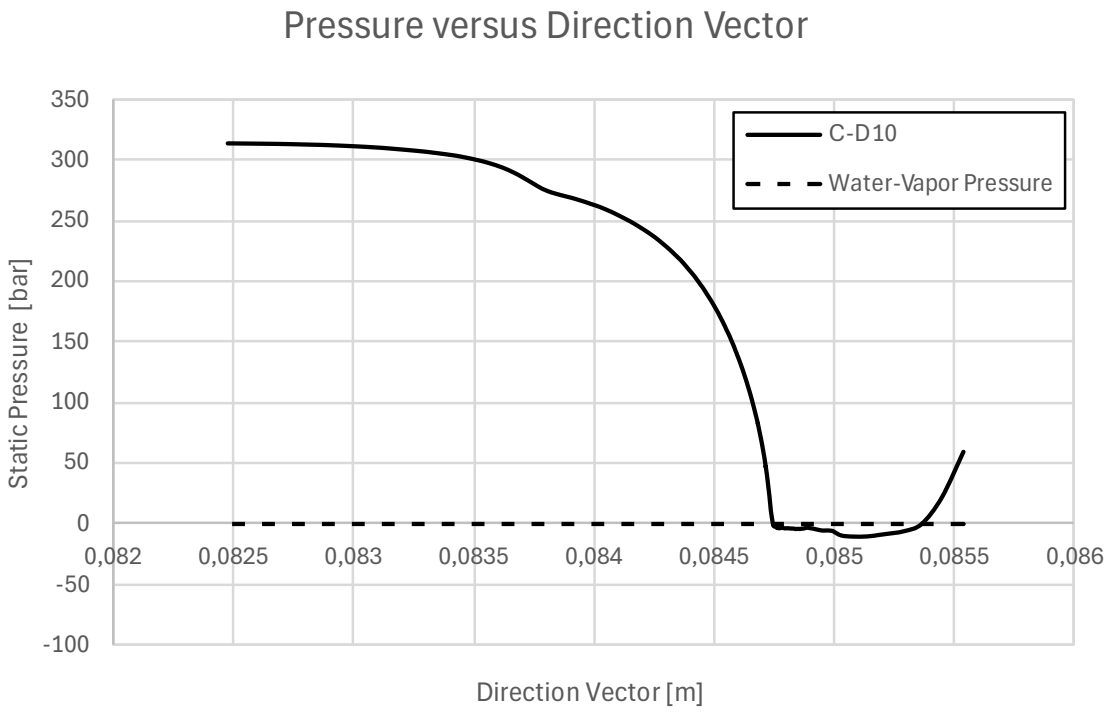

Figure 3.2 Static pressure across a line through the orifice section of C-D10

Cavitation can be assessed by identifying regions where the pressure falls below the vapor pressure in a single-phase flow. In Figure 3.3, such regions are indicated by a black-and-white scale overlaying the conventional pressure contour. Although the precise magnitude of cavitation cannot be determined without a multiphase simulation, it is evident that

cavitation is likely to occur in the zone between the seat and the poppet, where it would be costly to modify the valve components. Furthermore, the occurrence of cavitation is not symmetrical due to the valve's geometric configuration. While an initial consideration might suggest that a back pressure of 5 bars, located closer to the left-hand side, could mitigate cavitation. However, it is not the case as it is observed that a greater zone falls below the vapor pressure in the left-hand side. This is primarily due to the more pronounced vortex dynamics on the left-hand side, which overshadow the potential benefits of the back pressure in reducing cavitation.

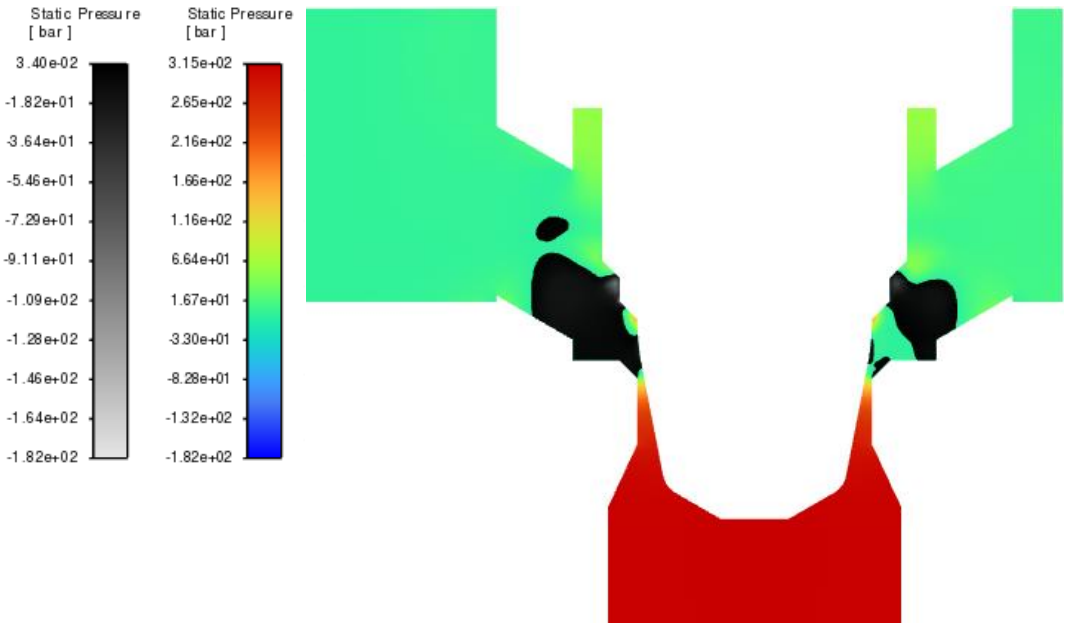

Figure 3.3 Static pressure contour with highlighted regions where the pressure falls below the vapor pressure of C-D10

Due to the pressure being able to drop below the vapor pressure, the flow rate is over predicted by Fluent, although not to a major extent in this case since the discharge coefficient is expected to be close to 1 as no separation of flow is observed at the orifice section. Hence, the only solution to obtaining the correct flow rate is to run the simulation with the multiphase model enabled. Flow rate and the corresponding discharge coefficient are provided in Table 8 below.

Table 8 Results of C-D10 case

Case	Volumetric Flow Rate, Q [L/min]	Discharge Coefficient, C_d
C-D10	1967.33	0.93

Closer to the restricted area, velocity increases a great amount and reaches its maximum at the vena contracta, which is approximately 266 m/s. Vortices of different magnitudes can be observed downstream of the orifice, shown in Figure 3.4. Apart from the pressure information, also the vortices give a vast idea of where cavitation may occur since they create regions of low pressure in a flow. In a vortex, the lowest pressure is typically found at the core, making it the region where cavitation is most likely to initiate [14]. The reason for an asymmetric cavitation in the symmetry plane is more evident after an investigation of the magnitudes of the vortices formed. Moreover, it is possible to observe (Figure 3.4 and 3.5) that the flow does not separate passing from the orifice section due to the geometry of the valve and the direction of the flow.

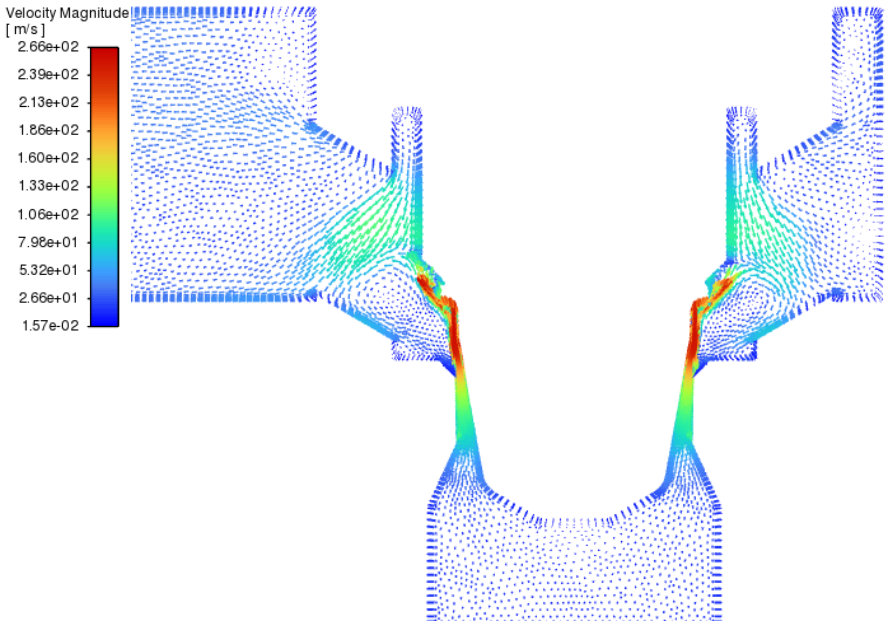

Figure 3.4 Velocity vectors of C-D10

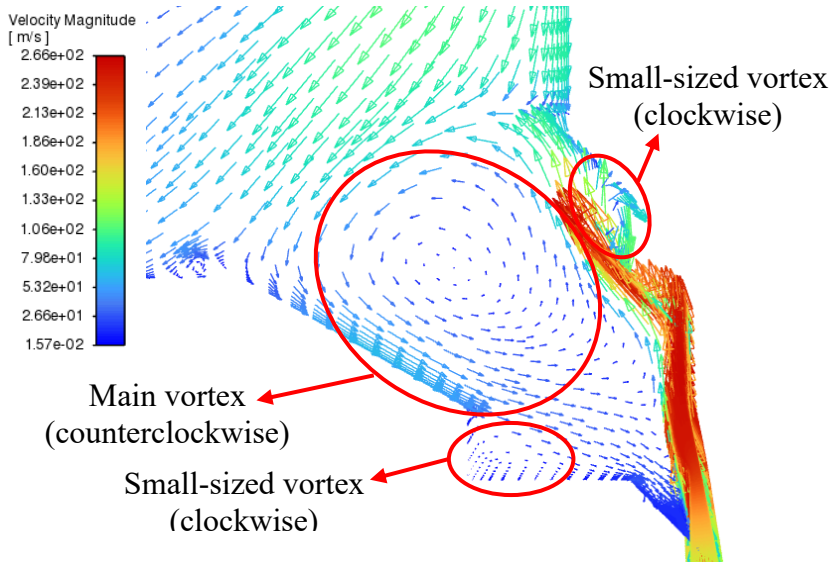

Figure 3.5 Velocity vectors of C-D10 in close-up view

3.2 Effect of valve geometry on cavitation

Prototype valve designed by HTS S.r.l is analyzed in terms of cavitation reduction with respect to the commercial valve. Prototype valve aims to create a gradual pressure drop in two sections: restricted area of the valve and through the tubes connecting the restricted area to the outlet section, where lies the cartridge. This should help the pressure to not fall below the vapor pressure of water. In addition, the cavitation occurrence can be transported to where the tubes are, so that in case of damage, only the cartridge can be substituted. Moreover, the simulations for the prototype valve are done in terms of equal flow rate instead of the opening of the valve because after the first prototype valve simulation, it is deducted that the flow is more restricted passing through the cartridge holes than the conical zone, shown in Figure 3.6. This results in a lower flow rate at the same opening of the valve. Since the pressure drop across the valve, and therefore cavitation, is highly dependent on flow rate, the analysis is conducted with the same flow rate, that of the commercial valve for both flow directions. Thus, the prototype valve is raised to allow for a greater flow rate, to an opening of around 15 millimeters.

.

In Figure 3.6 it is seen that the pressure drop across the conical zone is not so significant as in the case of the commercial valve. Instead, the flow is restricted at the holes of the cartridge thus the negative pressure zones are transported away from the poppet and the seat. However, a small amount of pressure drop is still observed to be considered for the discharge coefficient, although the desired gradual pressure drop effect is not obtained, and the pressure mainly drops around the cartridge.

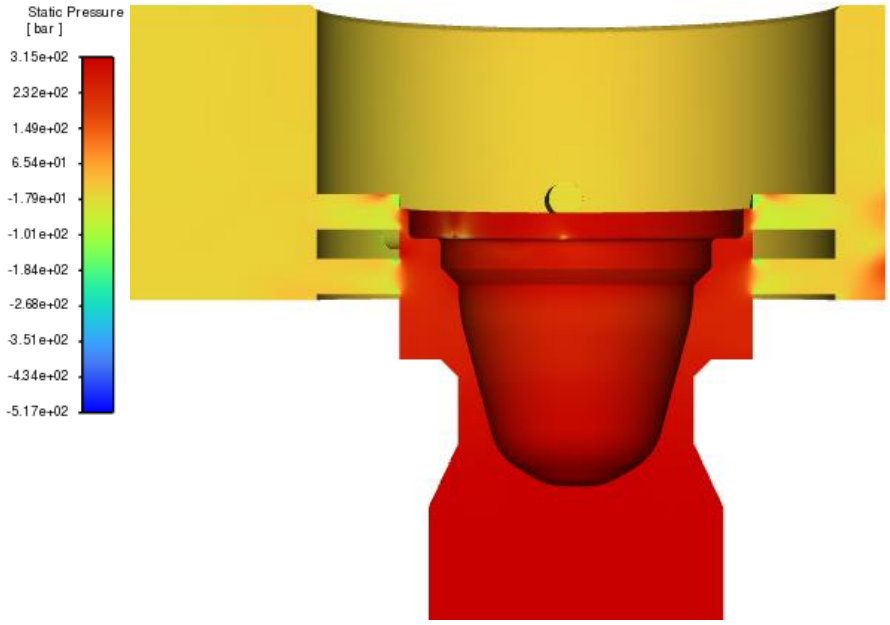

Figure 3.6 Static pressure contour of P-D10

In Figure 3.7, the flow pattern is shown through the velocity contour. Since the fluid enters the tubes in an angled manner, the real minimum area is tedious to calculate for each tube. The complete available areas for the tubes can be considered while calculating the discharge coefficient to give a general idea. All in all, for a qualitative study between two valves, the exact value of the discharge coefficient is out of interest.

In addition, it is observed that the maximum velocity is greater with respect to the commercial valve with 293 m/s. The flow accelerates a little through the conical zone and reaches its maximum in the tubes at the top because the flow is better guided to the top tubes instead of the tubes at the bottom.

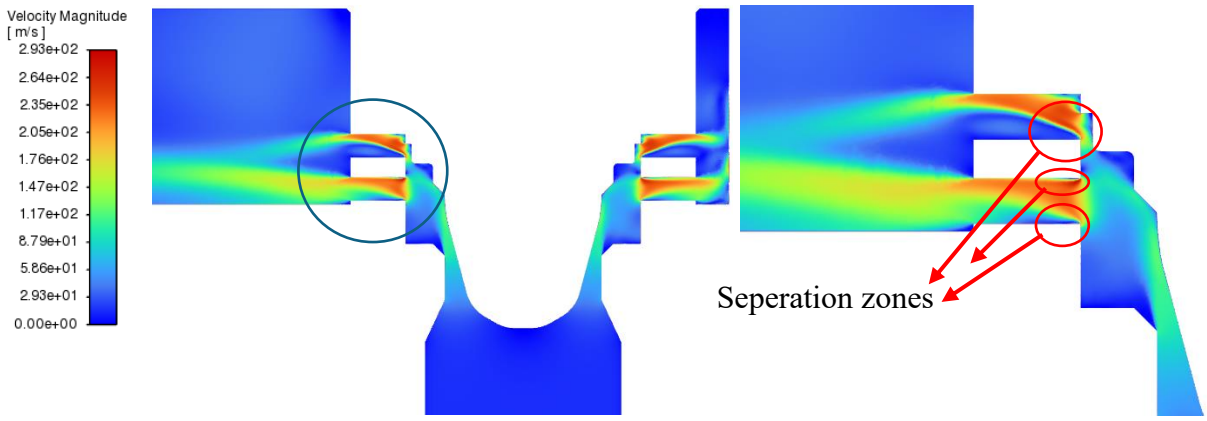

Figure 3.7 Velocity contours of P-D10

The results of both valves are provided in Table 9. As stated before, the area of passage for the tubes are lower than that is used during calculation. It is plausible that the discharge coefficient is reduced for the prototype valve, due to the separation zones that are formed at the entrance of the tubes, as the vena contracta effect is more pronounced.

Table 9 Results of P-D10 case

Valve Type	Opening $[mm]$	Flow Rate $[\frac{L}{min}]$	Maximum velocity $[\frac{m}{s}]$	Discharge coefficient, C_d
C-D10	10	1967.33	266	0.93
P-D10	15.5	2093.58	293	0.77
Δ [|%|]		6.42%	10.15%	17.2%

The zones that fall below the water vapor pressure are given in Figure 3.8 for both cases. It is deducted that although the prototype valve eliminates cavitation around the conical zone, it also transports it to the outlet section of the valve, which results in the same problem of

changing parts, this time for the valve body. Moreover, cavitation is more significant on the top-level tubes since it is previously evidenced that the velocity is higher than in the bottom-level tubes, resulting in lower pressure and greater separation also due to the direction of the flow how it enters the upper tubes.

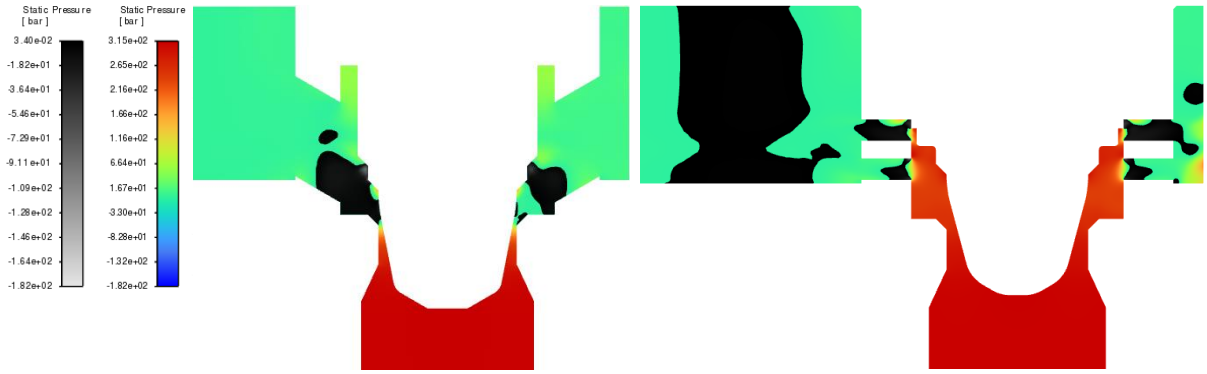

Figure 3.8 Static pressure contours of C-D10 and P-D10 with negative pressure zones highlighted

To mitigate the cavitation occurrence at the outlet section of the prototype valve, a new valve body has been developed by HTS S.r.l., that works only for diverging flow since the changes made to the body are located downstream of the tubes. Hence, in converging flow, the fluid will pass through the substituted section before being restricted, shown in Figure 3.9. The new body differs from the regular one mainly by its filleted geometry that eliminates sharp edges around the cartridge zone.

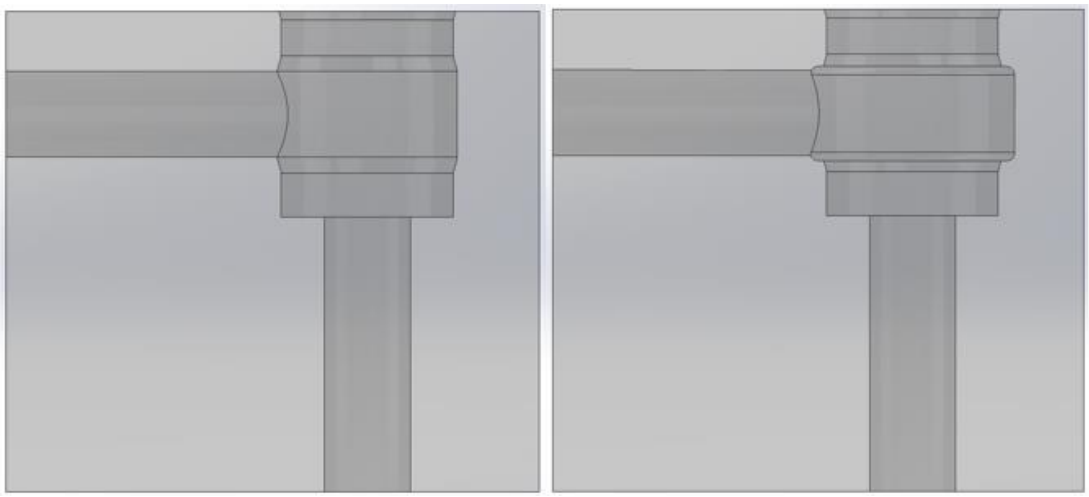

Figure 3.9 Commercial (left) and new valve body developed to mitigate cavitation at the outlet section (right)

The results presented in Figure 3.10 demonstrate that the new valve body significantly reduces cavitation presence at the outlet. The remaining zones apart from the tubes under the vapor pressure are due to separation of flow and vortices formed downstream of the tubes, as shown in Figure 3.11.

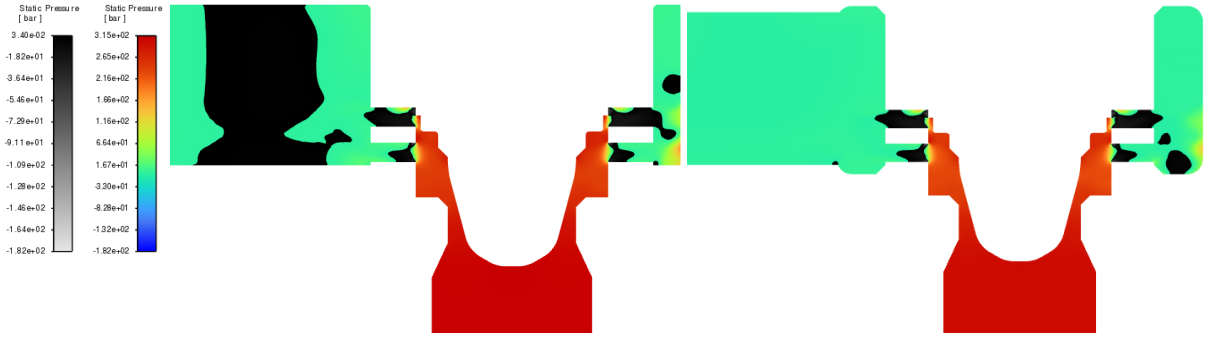

Figure 3.10 Static pressure contours of (a) P-D10 and (b) P-D10 with a new valve body with negative pressure zones highlighted

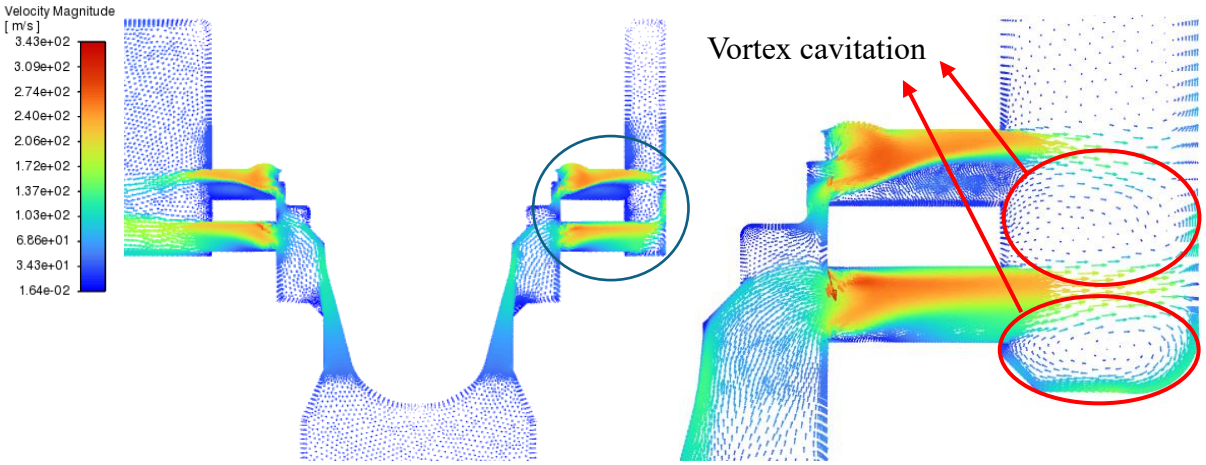

Figure 3.11 Formation of vortices in P-D10

3.3 Effect of flow direction on cavitation

Flow direction is of great importance when dealing with valve cavitation since most valves do not consist of symmetrical features, as a result, the guidance of the flow by the valve differs depending on the direction of the flow. Static pressure contours for the two directions of flow and the two valves are provided in Figure 3.12.

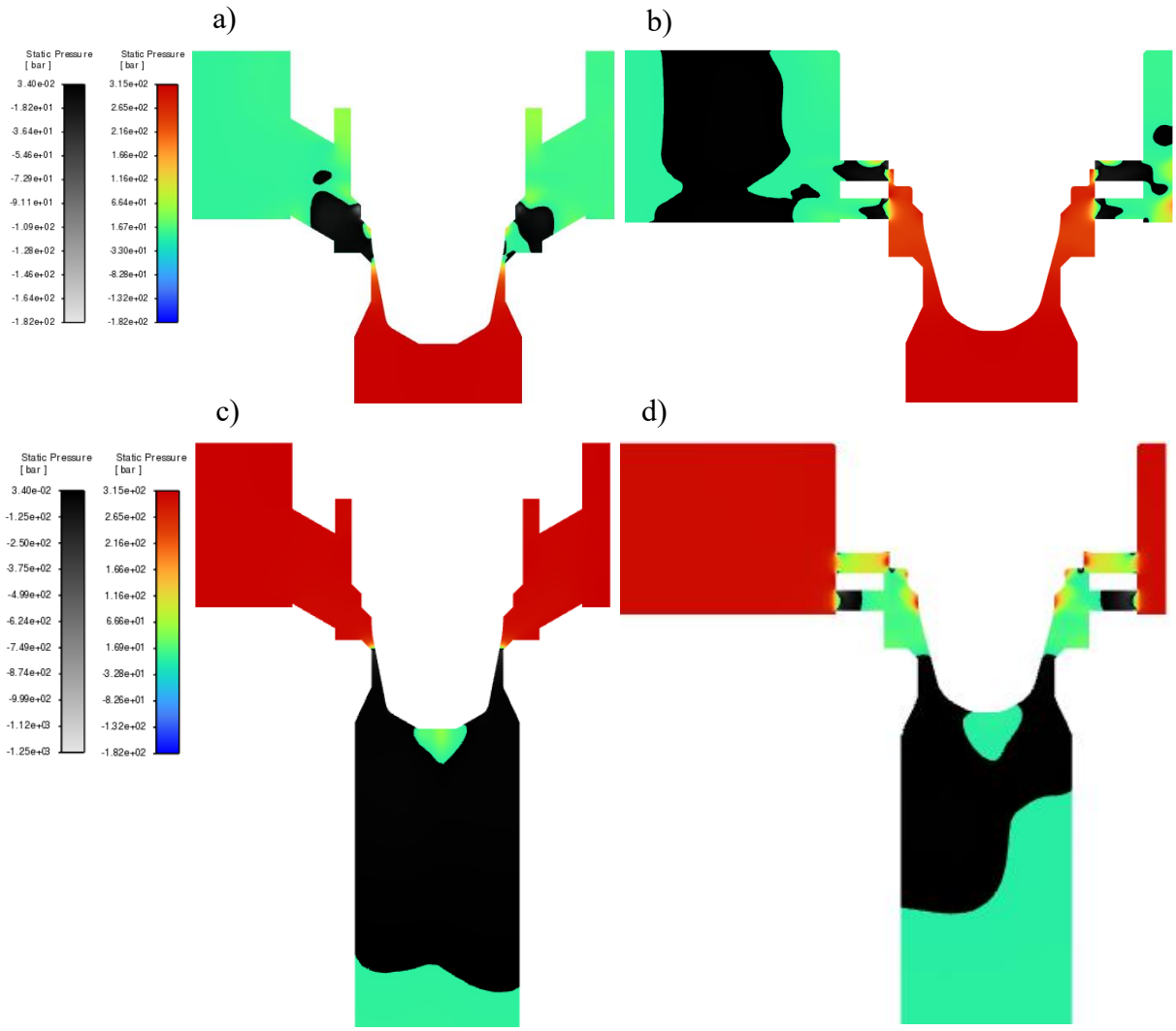

Figure 3.12 Static pressure contours of (a) C-D10, (b) P-D10, (c) C-C10 and (d) P-C10 with zones that fall below the vapor pressure highlighted

Firstly, cavitation is considerably more critical in converging flow than in diverging flow. It has been observed that the pressure downstream of the restricted area almost entirely drops below the vapor pressure of water, extending significantly toward the outlet— a phenomenon not observed in diverging flow. Secondly, the performance of the prototype valve is better in terms of the magnitude of the extension to the outlet, while cavitation is first expected to appear in the tubes of the cartridge. However, the improvement desired from the prototype valve is not apparent to be able to prefer the prototype to the commercial valve. Furthermore, in converging flow, the flow rate is over-predicted to a greater extent than in diverging flow, resulting in a larger opening of the prototype valve, as presented in Table 10.

Table 10 Results of C-D10, P-D10, C-C10 and P-C10 cases

Valve Type	Opening $[mm]$	Flow Rate $[L/min]$	Maximum velocity $[m/s]$	Discharge coefficient, C_d
C-D10	10	1967.33	266.27	0.93
P-D10	15.5	2093.58	293.81	0.77
C-C10	10	2403.16	450.42	1.13
P-C10	18.5	2627.32	316.93	0.72

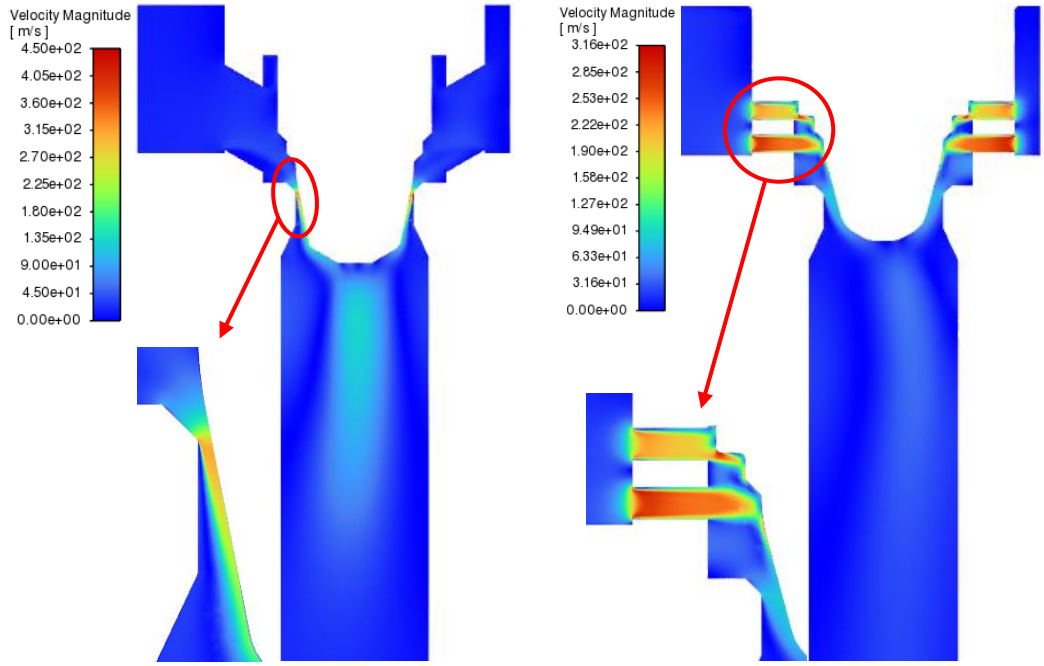

Figure 3.13 Velocity contours of C-C10 (left) and P-C10 (right)

In Figure 3.13, the reason for such an over-prediction can be observed. The valve does not follow the flow pattern in case of diverging flow and as a result, the flow separates. Such a separation at the minimum area of the valve causes the pressure to collapse to negative values around -1200 bar, when in real-life it corresponds to extremely critical cavitation phenomena. This also can be understood from maximum velocity on the symmetry plane, which is 450.42 m/s. On the other hand, for the prototype valve, since the minimum area is located at the tubes of the cartridge, the flow is sufficiently directed by the valve, particularly for the first set of tubes closer to the inlet section. In addition, since the flow is greatly accelerated in the tubes instead of the poppet-seat section, the accelerated flow does not arrive until the outlet section, so that pressure is not reduced as much as in the commercial valve, resulting in a better response to cavitation extension to the outlet. Overall, it is deduced that cavitation is more dangerous in converging flow for these configurations and no significant improvement has been noted for the prototype valve.

3.4 Effect of valve opening on cavitation

In this section, different spool openings of the proportional valve are investigated to analyze how cavitation characteristics are affected by it. Considering that the inlet and outlet parameters are kept constant, if the valve opening is increased, flow rate also increases, due to the enlargement of the minimum area where the fluid flows. The valve opening will be investigated case by case for each combination of valve and flow type.

Commercial valve, diverging flow:

In Figures 3.14, 3.15 and 3.16, pressure contour of the symmetry plane, three-dimensional view of the zones where the pressure is below the vapor pressure and the velocity vectors downstream of the throat are shown respectively for C-D5 and C-D10 cases. It is seen that the cavitation is more pronounced for 10-millimeter opening case as a greater surface is under the vapor pressure of water in C-D10. It also arrives further downstream of the throat, expanding through the holes of the cartridge. In Figure 3.16, the vortices are observed between the throat and the holes of the cage formed due to the accelerated flow exiting the throat, that creates low-pressure zones, which are the reason for the occurrence of cavitation phenomena.

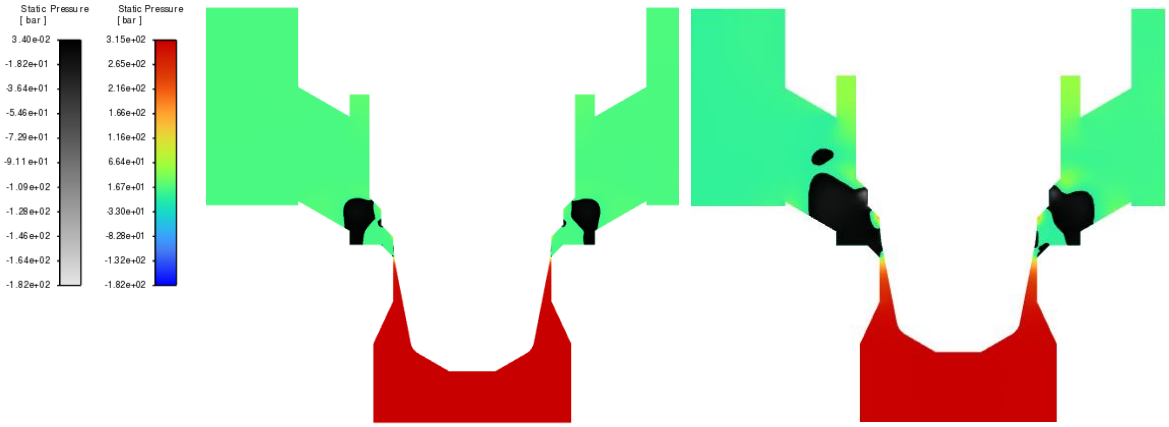

Figure 3.14 Pressure contours of C-D5 (left) and C-D10 (right)

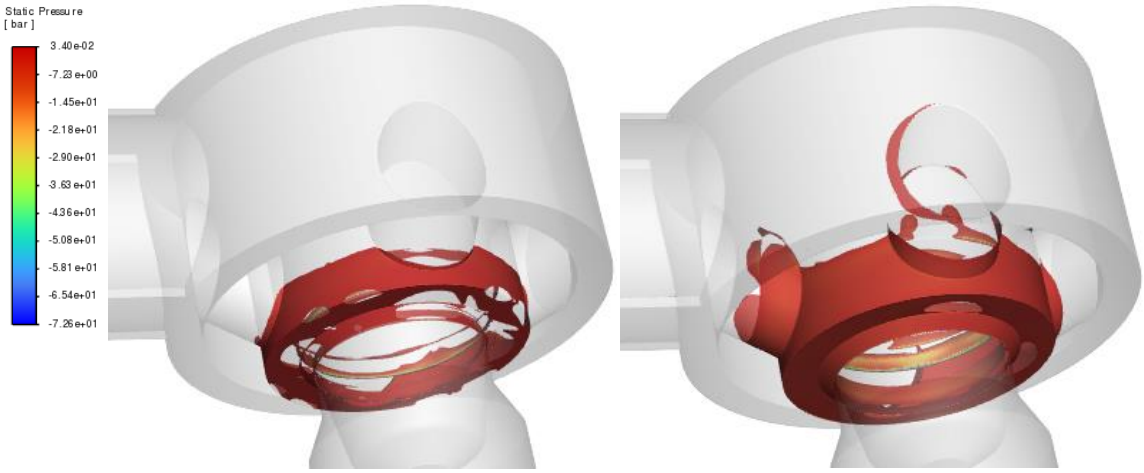

Figure 3.15 Pressure contour in 3D view of zones under possible cavitation of C-D5 (left) and C-D10 (right)

For openings of 20 millimeters and 40 millimeters, the maximum allowable flow rate through the valve is specified as 2500 L/min, with the outlet pressure maintained at a constant value of 5 bar as in all cases. This process is done to investigate the inlet pressure values, as well as the response of the valve to cavitation, since for openings over 10-millimeters the maximum flow rate is exceeded.

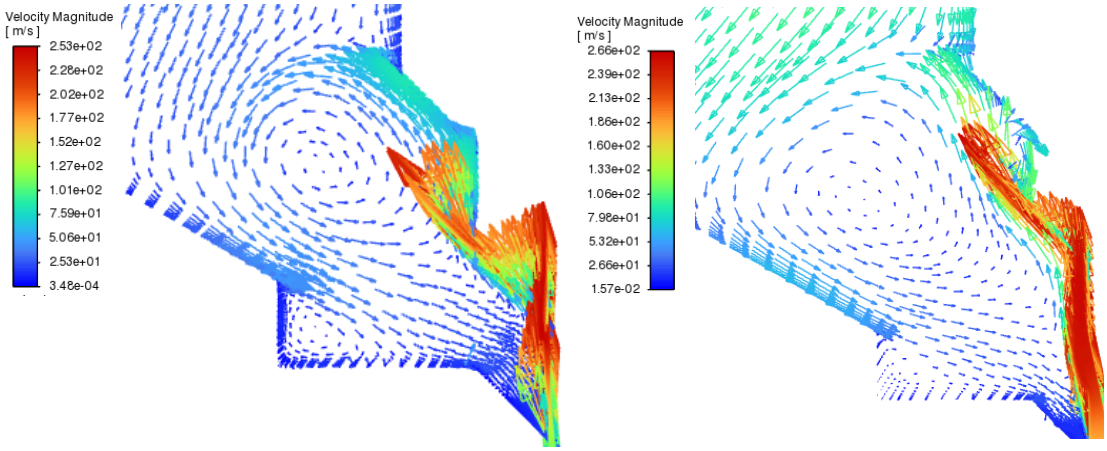

Figure 3.16 Velocity contours downstream of the throat of C-D5 (left) and C-D10 (right)

Firstly, in Figure 3.17, it is noted that in the maximum opening of the valve (40-millimeters), the throat between the poppet and the seat disappears and the pressure drop across the orifice is no longer observed. The valve is mainly under positive values of pressure, apart from a small section in the holes of the cage where separation is observed. The same situation applies for 20-millimeter case, although the region below the vapor pressure is greater due to the higher pressure drop across the valve caused by the lower minimum area of flow. Higher pressure drop results in a faster flow through the orifice, increasing the effect of the vortex. Moreover, inlet pressure is lower for 40-millimeter case (18.78 bar) which is related to the minimum area through the valve, by the square-root of the pressure drop, while pressure at the inlet for C-D20 corresponds to 80.96 bar.

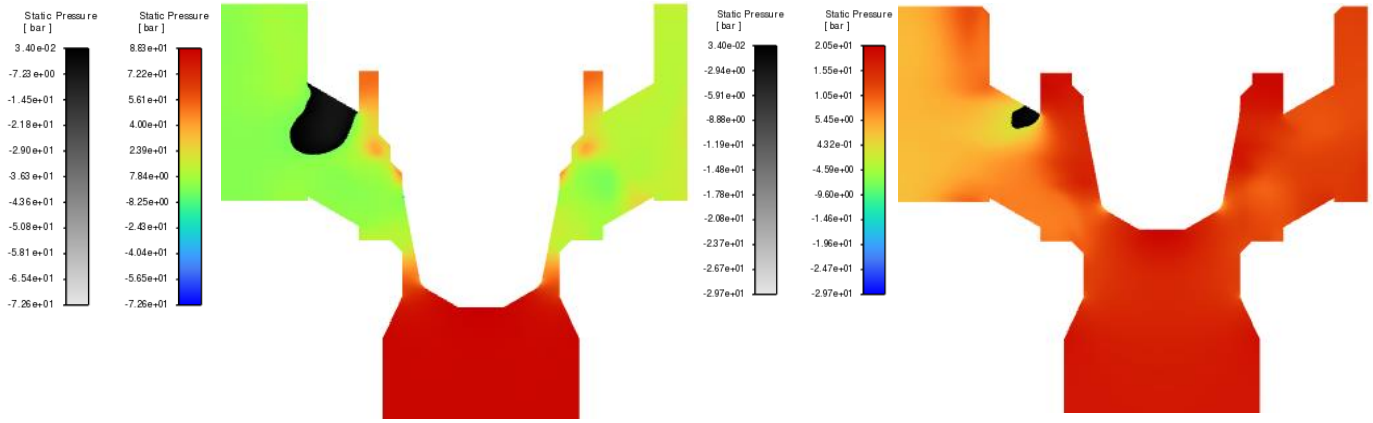

Figure 3.17 Pressure contours of C-D20 (left) and C-D40 (right)

In Figure 3.18, the zones under possible cavitation are illustrated for 20- and 40- millimeter openings respectively. It is seen that the zones under possible cavitation are downstream of the holes in the cartridge, which are faced to the outlet section as the direction of the flow. Moreover, for C-D20, cavitation can be expected around the throat as well.

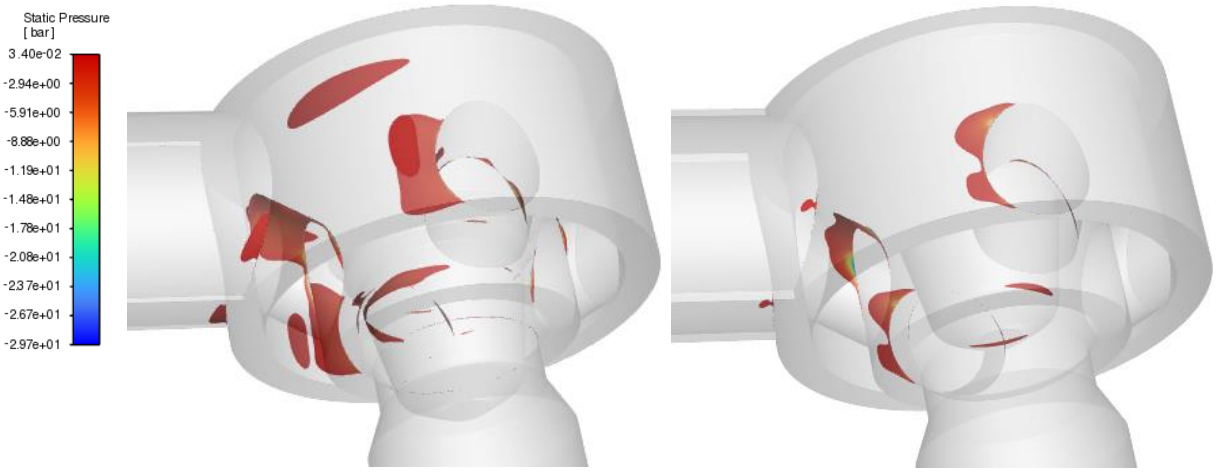

Figure 3.18 Pressure contour in 3D view of zones under possible cavitation of C-D20 (left) and C-D40 (right)

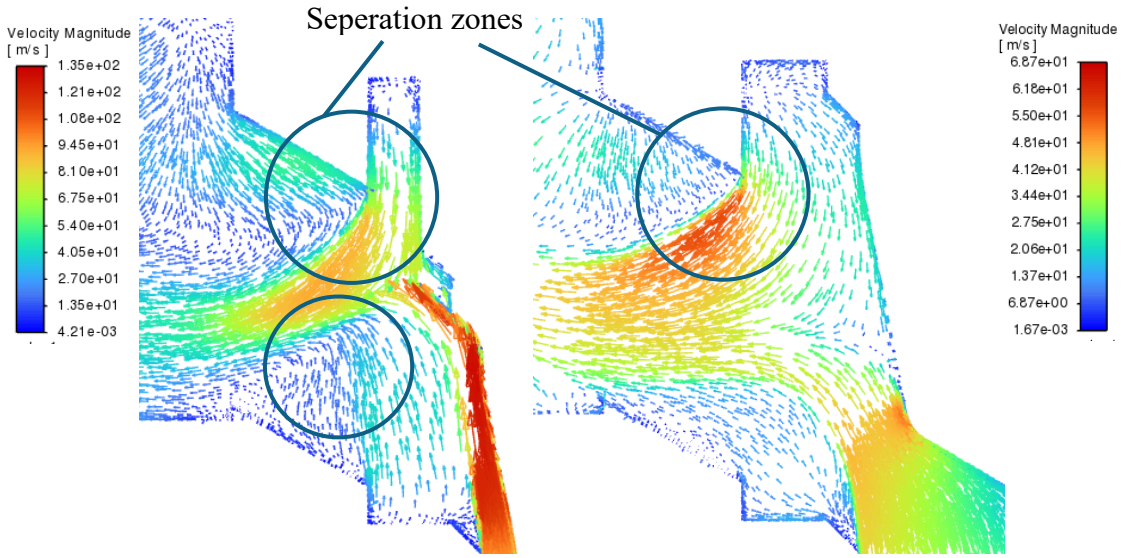

Figure 3.19 Velocity contours downstream of the throat of C-D20 (left) and C-D40 (right)

In Figure 3.19, velocity vectors are depicted to show the possible formation of vortices. The maximum velocity at the symmetry plane in the C-D20 configuration is nearly twice as high

as that observed in the maximum valve opening case. Specifically, in the C-D20 configuration, the velocity reaches 135 m/s, whereas in the C-D40 configuration, it is approximately 66 m/s. The separation zones are evident in both cases, which are located at the entrance of the holes in the cage. However, this type of cavitation is not a major issue due to its location, as the cage can always be changed easily, since it is not a principal component of the valve structure.

Prototype valve, diverging flow

In Figure 3.20, pressure contours are depicted along with the zones under possible cavitation.

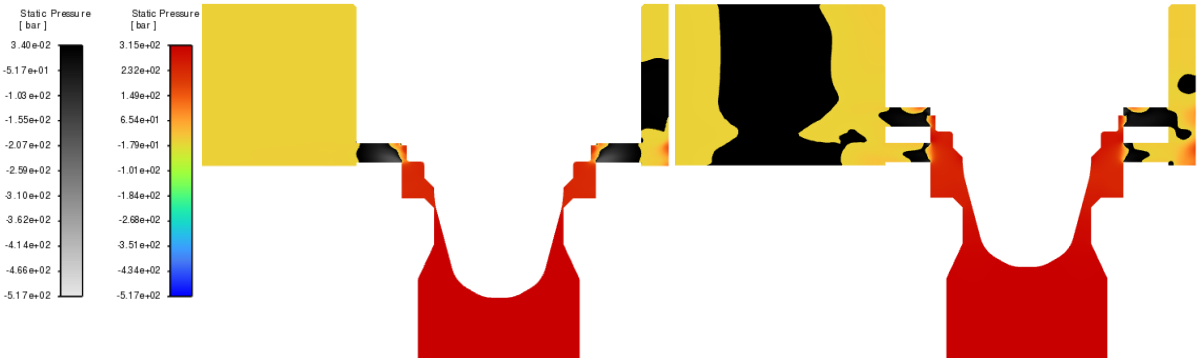

Figure 3.20 Pressure contours of P-D5 (left) and P-D10 (right)

In P-D5 case, a region under 0.034 bar is observed that is located at the opposite side from the outlet. This is due to the back pressure that is not able to reach that area where separation caused by the high velocity flow inside tubes is observed. Instead, for P-D10, the tubes are doubled, and so the flow is divided into two parts, together with their kinetic energy. Thus, separation is not as pronounced as the previous case.

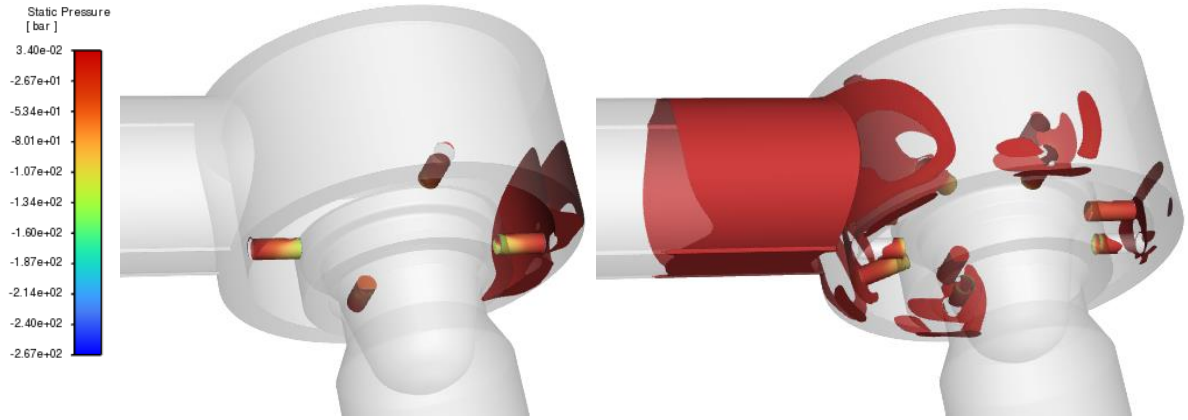

Figure 3.21 Pressure contour in 3D view of zones under possible cavitation of P-D5 (left) and P-D10 (right)

In Figure 3.21, pressure contours are illustrated through the three-dimensional view. It is evident that the P-D10 case is problematic in terms of cavitation extension to the outlet. Same behavior is also observed in commercial valve, however, since in that case cavitation occurs around the throat of the valve, it is only extended to the holes of the cartridge. Instead, for the prototype valve, the major pressure drop happens in the tubes through the holes, which is closer to the outlet section. It is more pronounced with respect to the commercial valve case due to the expansion to a larger domain. For the 5-millimeter case, cavitation is mainly focused on the holes of the cage which provides a better response with respect to the 10-millimeter opening.

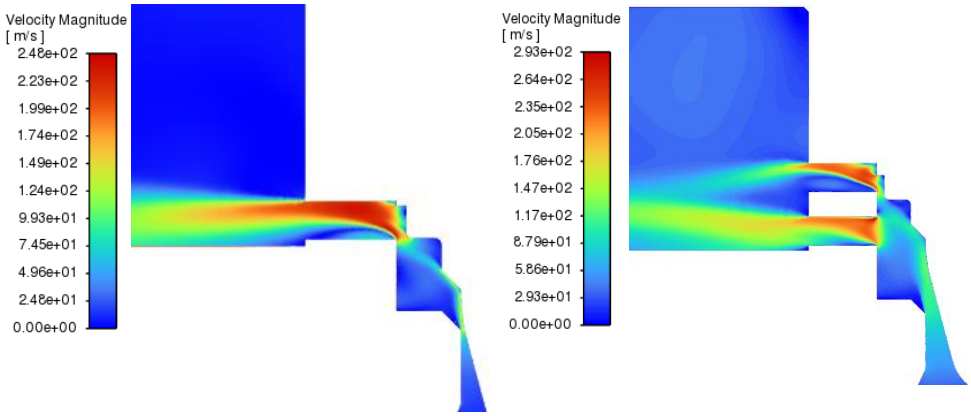

Figure 3.22 Velocity contours of P-D5 (left) and P-D10 (right)

In Figure 3.22, velocity contours instead of velocity vectors are shown for better clarity of the images, since depicting large velocity gradients in small tubes through vectors is difficult. The velocities between the two simulations are similar since the velocity depends

on the discharge coefficient and the pressure drop which is the same for both cases. It is possible to see the evolution of the fluid velocity and how the flow is guided more to the top-level tubes.

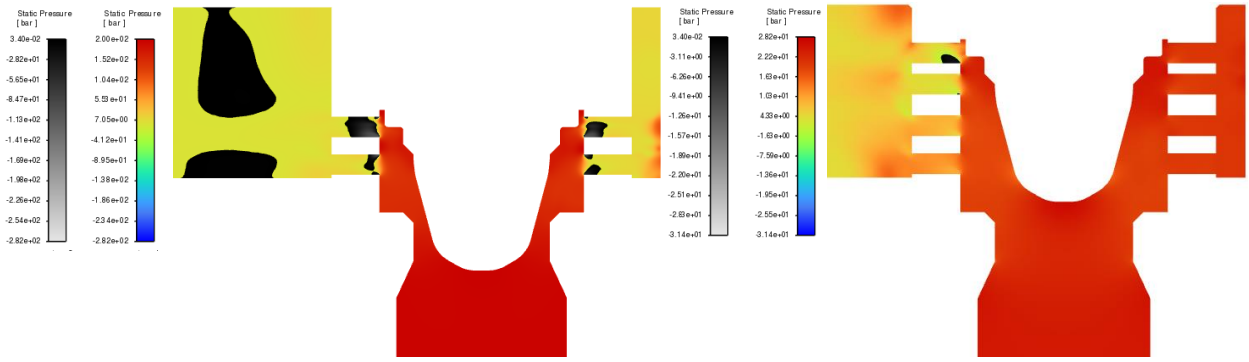

Figure 3.23 Pressure contours of P-D20 (left) and P-D40 (right)

Pressure contours of P-D20 and P-D40 are provided in Figure 3.23. Cavitation is reduced to a major extent in the maximum opening of the valve, since all the holes are now covered, and the flow is divided into more parts, seen in Figure 3.24, where a part of the second image is hidden due to privacy purposes. The small region where cavitation may be expected is formed due to the separation downstream of the tubes where they are connected to the outlet section. The only two tubes where the pressure goes below the vapor pressure are the first two levels facing the outlet, because it is where the flow is guided to, leading to

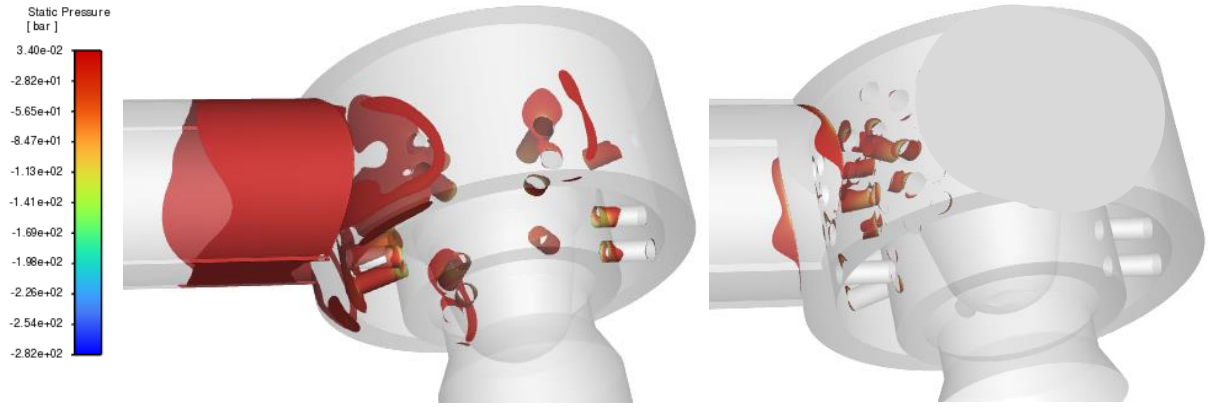

Figure 3.24 Pressure contour in 3D view of zones under possible cavitation of P-D20 (left) and P-D40 (right)

a high velocity. Whereas in P-D20 case the extension of cavitation is still observed, even though the pressure drop is decreased to 185.68 bar.

Moreover, due to geometry, the top-level tubes are more prone to separation, considering how the fluid enters the tubes, shown in Figure 3.25.

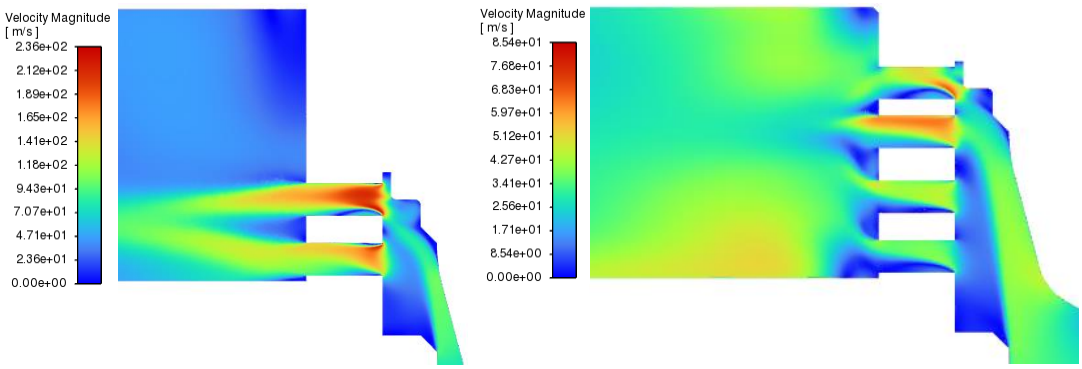

Figure 3.25 Velocity contours of P-C20 (left) and P-C40 (right)

Commercial and prototype valve, converging flow

The results of both commercial and prototype valve in converging flow are presented below. In this section, simulations for 20-millimeter and 40-millimeter openings are not conducted, as they serve the purpose to determine the inlet pressure at the maximum flow rate, which is already done for diverging flow.

In Figure 3.26, pressure contours of cases C-C5, P-C5, C-C10 and P-C10 are presented. The same behavior can be observed also for converging flow that as the opening of the valve is increased, the cavitation spreads to a greater area in both valves. The severity of cavitation cannot be accurately assessed through single-phase flow simulations. Hence, it is not possible to distinguish between regions with a vapor fraction of 0.1 and those with a vapor fraction of 0.9. It should be noted that the prototype valve responds better at the same flow rate with respect to the commercial valve. In converging flow, the intended two-step restriction of the prototype valve functions almost as intended. Initially, the flow enters the tubes, drops below the vapor pressure, and then partially recovers before being further restricted at the throat, where the cavitation area is relatively smaller.

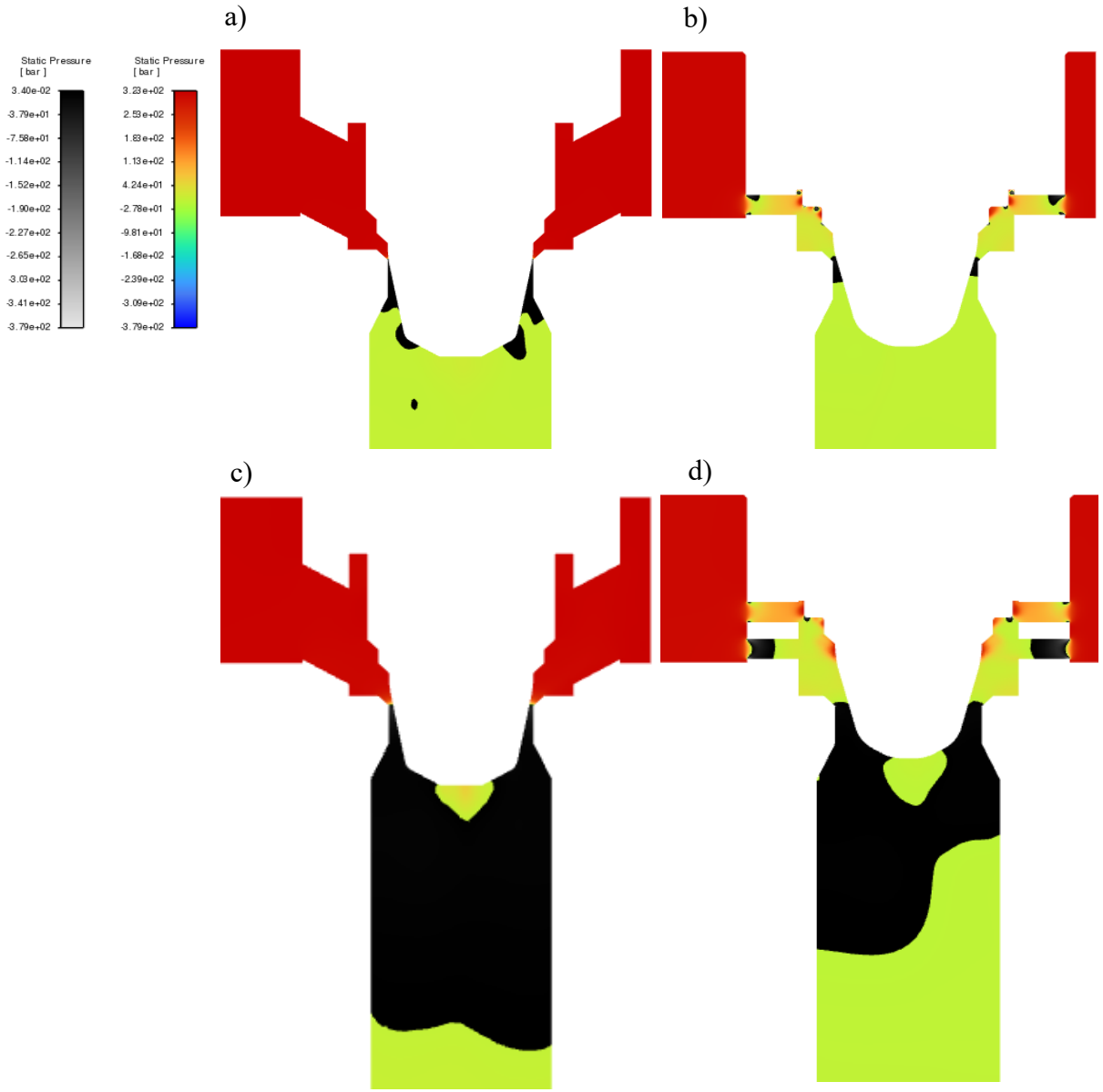

Figure 3.26 Pressure contours of (a) C-C5, (b) P-C5, (c) C-C10 and (d) P-C10

The zones potentially subject to cavitation along the walls are illustrated in Figure 3.27, complementing the previous figures from the symmetry plane. These zones extend further along the walls compared to the symmetry plane, as the velocity is lower near the walls.

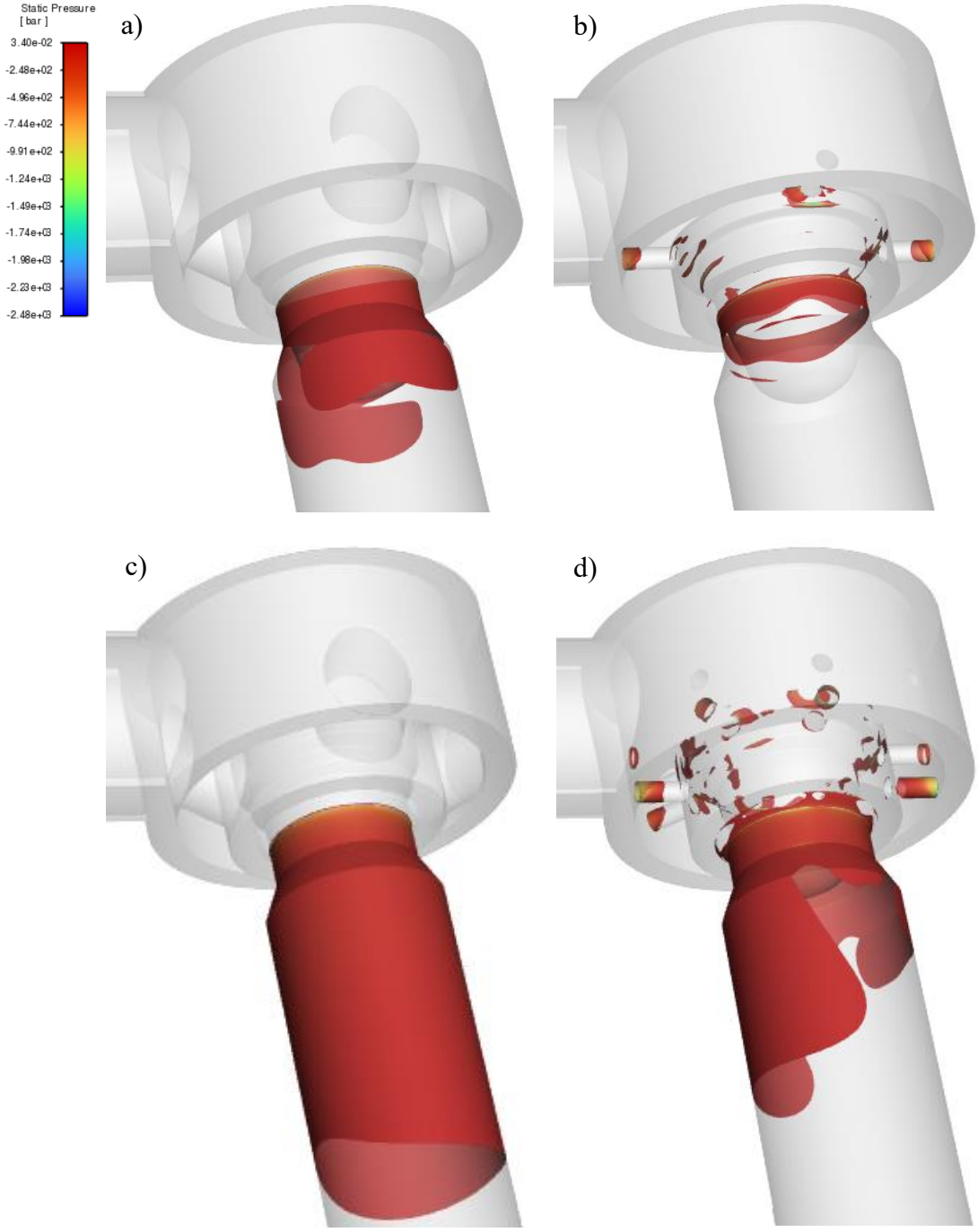

Figure 3.27 Pressure contour in 3D view of zones under possible cavitation of (a) C-C5, (b) P-C5, (c) C-C10 and (d) P-C10

The maximum velocity of the prototype valve is the same for both openings. Considering Equation (1), the pressure drop is equal for both cases and the flow rate changes proportionally to the minimum area of flow, meaning that the discharge coefficients are similar between the two cases. However, for the commercial valve, the maximum velocity is higher in the lower opening case, that may be due to the accelerated flow caused by the very small opening that faces the poppet. Thus, the flow is not as guided as in the prototype valve, and since the velocity is higher the separation is more pronounced for this case due to the adverse pressure gradient, although the cavitation is not extended further in the outlet, it may be said that the cavitation should be more severe than the 10-millimeter opening case.

The results of all 12 simulations conducted for this study are presented below in Table 11.

Table 11 Flow simulation results of all 12 cases

Opening [mm]	Flow Type	Valve	Volumetric Flow Rate [L/min]	Pressure Drop, ΔP [bar]	Discharge Coefficient, C_d [-]
5	Diverging	Commercial	514.52	310	0.98
		Prototype (6.2 mm)	511.74	310	0.55
	Converging	Commercial	819.66	310	1,57
		Prototype (8.4 mm)	839.62	310	0.61
10	Diverging	Commercial	1967.32	310	0.92
		Prototype (15.5 mm)	2093.58	310	0.67
	Converging	Commercial	2439.36	310	1,13
		Prototype (18.4 mm)	2627.32	310	0.68
20	Diverging	Commercial	2500	75.96	0.91
		Prototype	2500	185.68	0.69
40	Diverging	Commercial	2500	13.78	0.63
		Prototype	2500	19.66	0.45

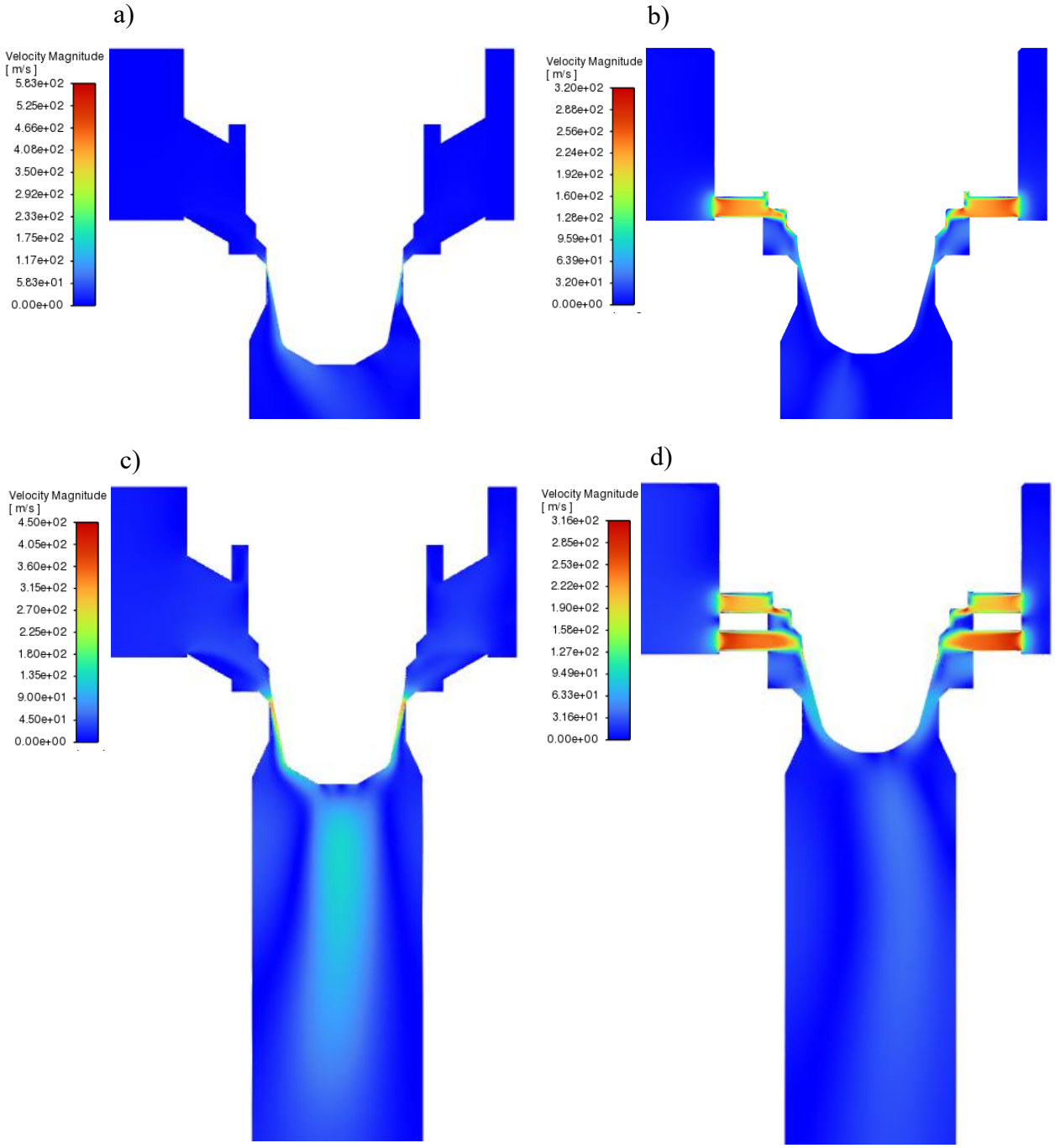

Figure 3.28 Velocity contours of (a) C-C5, (b) P-C5, (c) C-C10 and (d) P-C10

3.5 Comparison of single-phase and multiphase flow simulations

A multiphase simulation is run for C-C10 to analyze both the similarities and differences between the two methods considered for cavitation suggested by literature, as well as to obtain the correct volumetric flow rate through the valve, so that the magnitude of the over-estimation of the flow rate is determined. In Figure 3.29, vapor volume fraction contour of the multiphase simulation is provided together with the static pressure contour of the single phase, where the analysis is based on in this study.

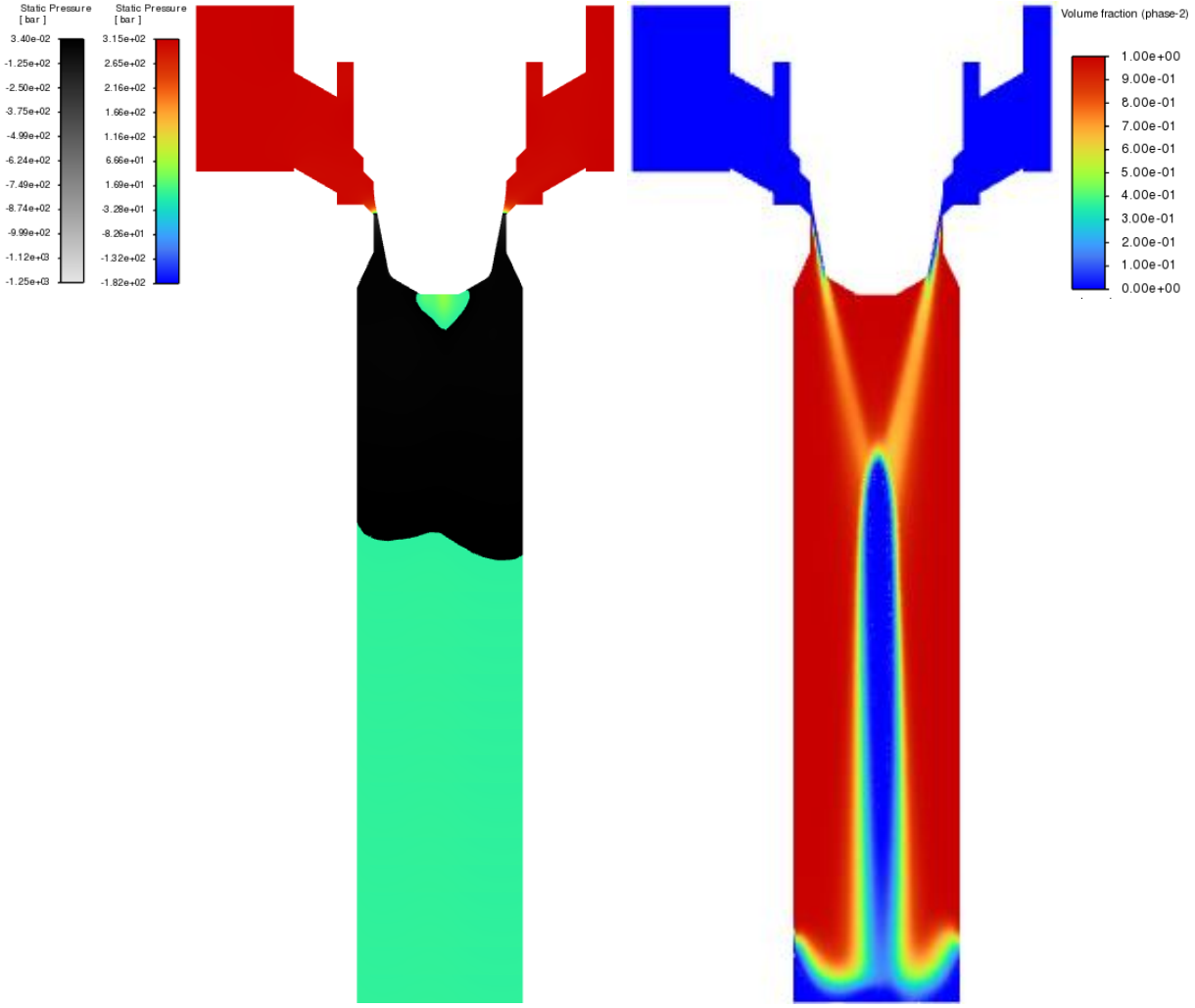

Figure 3.29 Static pressure contour in single-phase (left) and vapor volume fraction in multiphase flow (right) of C-C10

In the multiphase simulation, it is observed that the first vapor bubbles form due to the separation of the flow when the fluid first enters the restriction. Meanwhile, in the high-velocity liquid jet, accelerated by the restriction, vapor bubbles begin to form, although it does not completely become filled with vapor. Then, it recovers to form a liquid-filled cylindrical region around the centerline of the outlet, which connects to the outlet boundary where the improvement in terms of liquid fraction of the 5 bar pressure is seen. Apart from the cylindrical volume, the outlet is almost completely filled with vapor with a fraction above 0.9. The single-phase simulation is able to capture the beginning of cavitation, however it greatly underestimates its extension to the outlet. In addition, the acceleration of the jet through the outlet is ignored and consequently the magnitude of the vortex cavitation at the bottom of the poppet. When considering cavitation in a single-phase flow simulation, static pressure contour should be considered together with the velocity contour, searching for the zones where vortices occur. The maximum velocity is reduced in multiphase simulation with a value of 310 m/s while for single-phase case it reaches around 507 m/s. The turbulent kinetic energy also decreases because a portion of the energy due to the pressure drop is spent during the phase-change operation from liquid water to water-vapor [10]. In Figure 3.30 the velocity vectors together with the vortices at the outlet section are shown and in Figure 3.31 turbulent kinetic energy contours are presented.

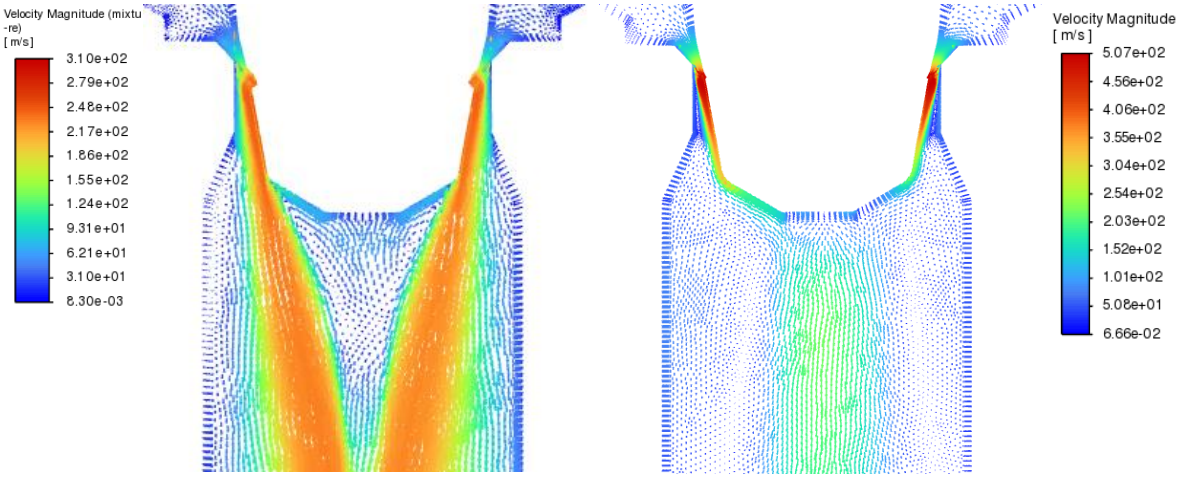

Figure 3.30 Velocity contours of multiphase (left) and single-phase (right) simulation of C-C10

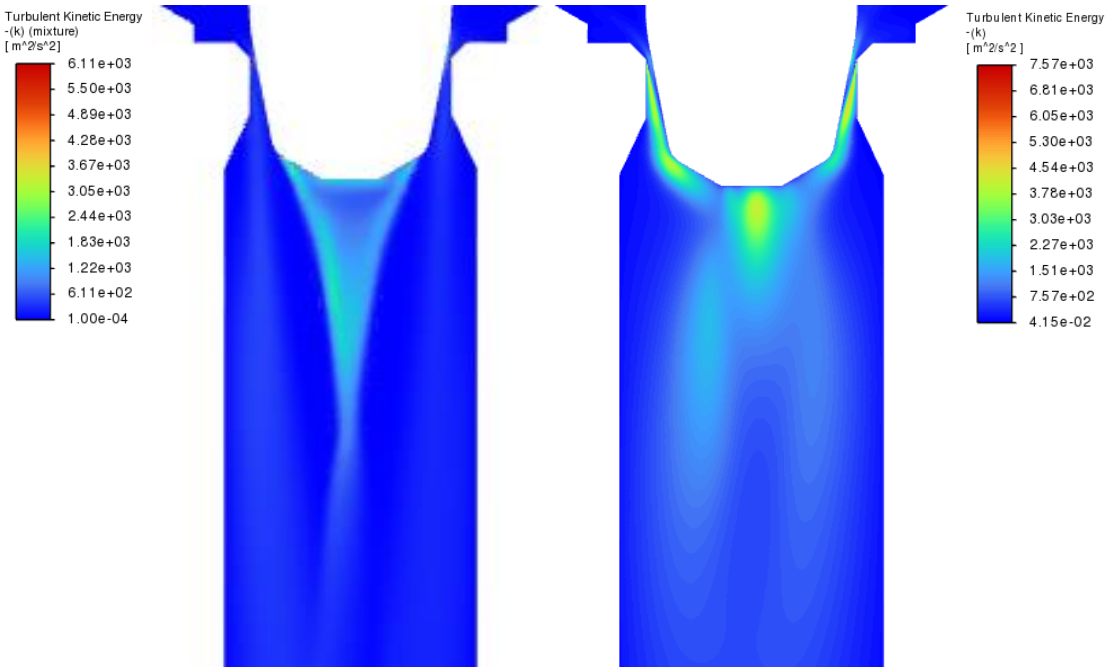

Figure 3.31 Turbulent kinetic energy contours of multiphase (left) and single-phase (right) simulations of C-C10

Moreover, the flow rate is also reduced for the same reason explained above. In multiphase simulation, the minimum pressure is limited by the vapor pressure of the liquid, thus the pressure drop remains unvaried. Therefore, the flow rate remains constant, and the flow is choked. Meanwhile in single phase flow there is no such lower limit, and the flow rate is characterized by the minimum negative pressure reached at the throat. A line through the throat is created to depict these two behaviors depending on the simulation choice, shown in Figure 3.32.

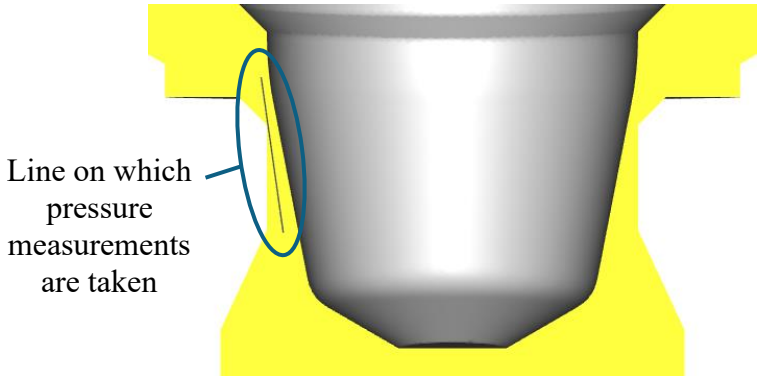

Figure 3.32 Line through the throat of C-C10

In Figure 3.33, the evolutions of pressure through the line located at the throat area are shown. Graph direction follows the flow direction. As seen, through the solid line corresponding to multiphase simulation, the pressure remains constant downstream of the minimum area, while for the single-phase flow the pressure keeps on decreasing to almost -250 bar.

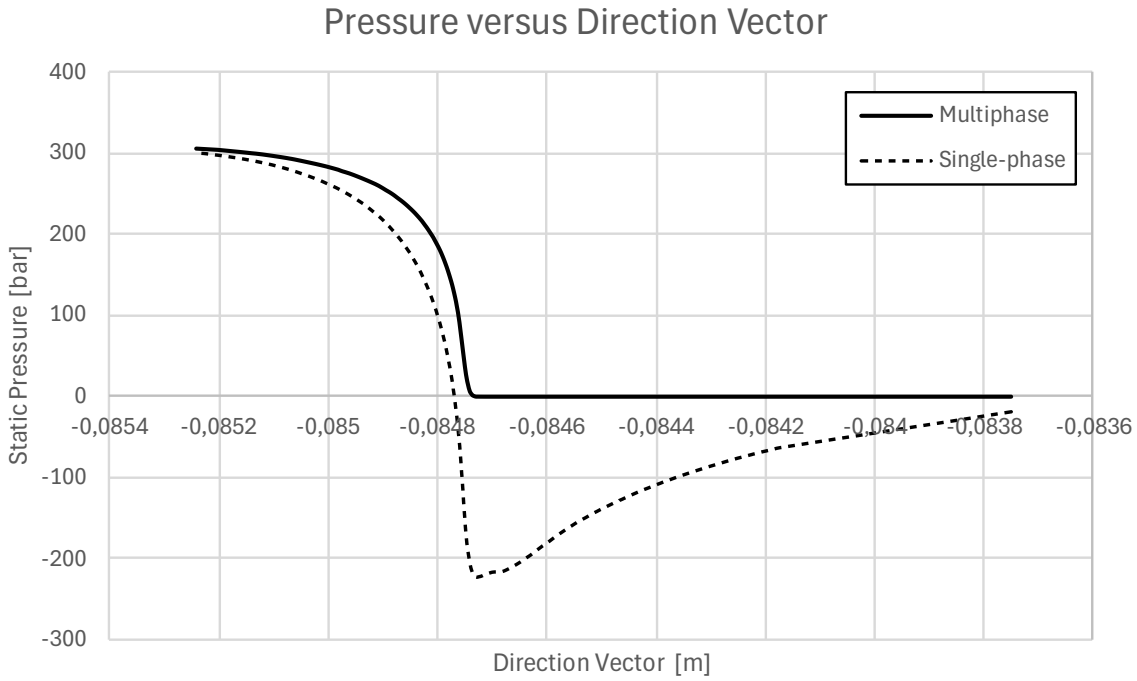

Figure 3.33 Static pressure vs position plot through the throat section of C-C10

The definitive flow rate is provided in Table 12 below. As foreseen, a reduction in the flow rate is observed by 45.69% and the new discharge coefficient is more sensible considering the separation caused by the geometry of the flow.

Table 12 Volumetric flow rate results for single-phase and multiphase simulations of C-C10

Simulation Type	**Volumetric Flow Rate, Q $[L/min]$**	**Discharge Coefficient, C_d**
Single-phase	2472.78	0.92
Multiphase	1697.26	0.65
Δ [|%|]	45.69	41.43

Additionally, a simulation to investigate the effect of outlet pressure on cavitation dynamics is conducted, since in Figure 3.29 it is seen that the cavitation volume impacts the 5 bar outlet pressure and consequently the bubble formation is stopped at an equilibrium boundary. Hence, the same multiphase simulation is run with 35 bar of outlet pressure. The vapor volume fraction contours are provided in Figure 3.34 below.

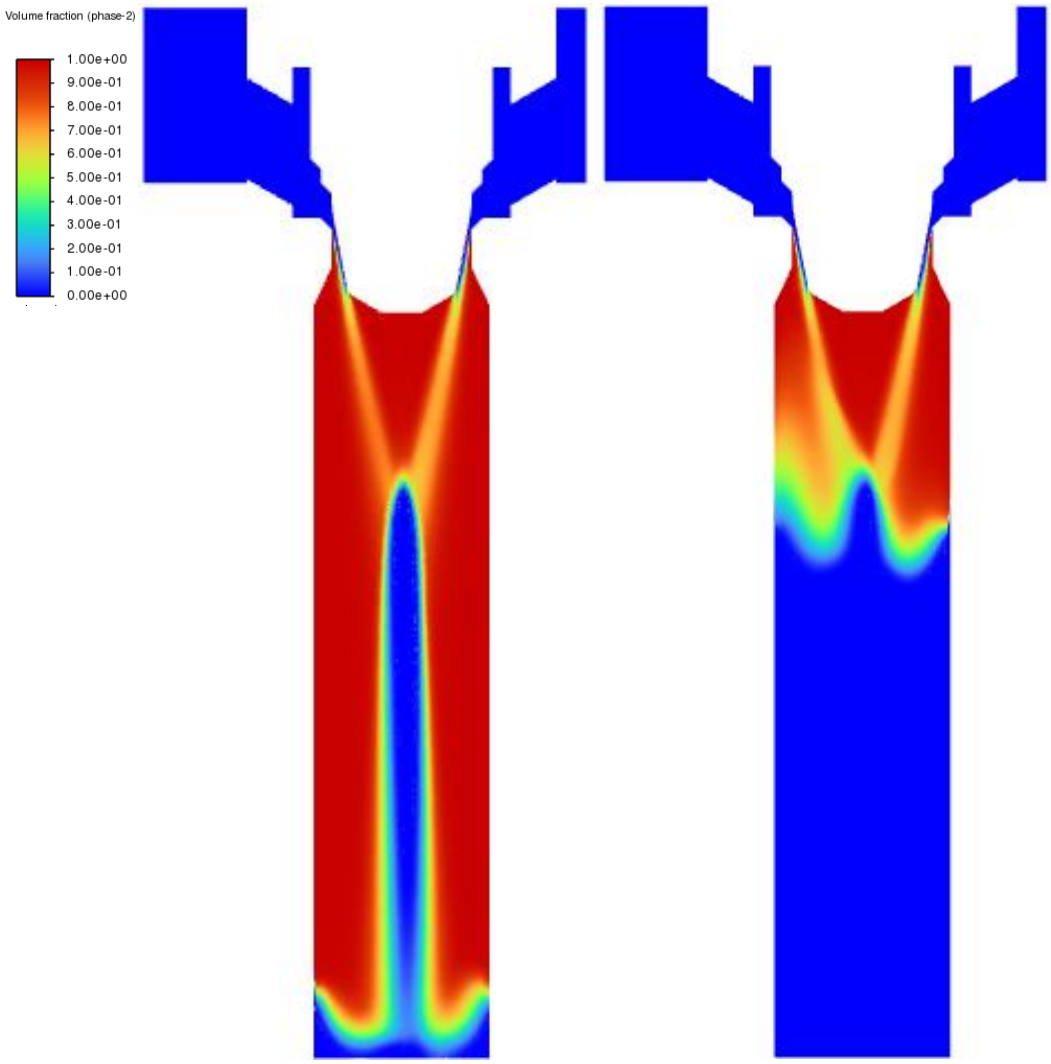

Figure 3.34 Multiphase simulation with outlet pressure of 5 bars (left) and 35 bars (right)

The boundary of the impact between the vapor due to the orifice and liquid due to the outlet pressure is transported closer to the throat as the outlet pressure increased 7 times. It is clear that, back pressure is one of the fundamental aspects to mitigate cavitation, however it is not enough in this case to reduce cavitation to a major extent, because of the valve geometry and the energy due to the high inlet pressure. On the other hand, it is perfectly plausible that the volumetric flow rate is the same for the two simulations, as the inlet pressure is not varied and the lower limit is defined by the vapor pressure of the liquid, and as a result, the pressure drop is equal.

In addition, a further multiphase simulation is conducted, building on the findings of [15], which suggest that when the cavitation percentage remains below a specific threshold, a single-phase simulation can adequately represent the regions affected by cavitation. This is achieved by utilizing the static pressure contour, which, in such cases, aligns perfectly with the results of the multiphase simulation. Thus, the case C-D20 is selected to conduct such analysis since it is a less severe case in terms of cavitation. The new results are presented together with the results of the single-phase simulation of the same case below in Figure 3.35.

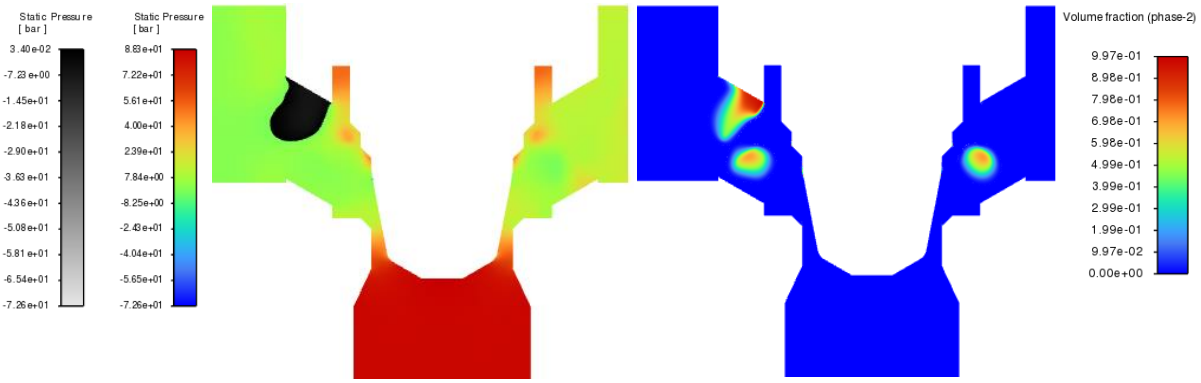

Figure 3.35 Static pressure contour in single-phase (left) and vapor volume fraction in multiphase flow (right) of C-D20

It is noted that the location and shape of the cavitation matches with the multiphase simulation, considering the vortices formed downstream of the throat as well. Inlet pressure results are provided in Table 13.

Table 13 Single and multiphase simulation results of C-D20

Simulation Type	**Inlet Pressure [bar]**
Single-phase	80.96
Multiphase	77.43
Δ [|%|]	4.36

It has been validated that single-phase simulation is suitable for modeling low-percentage cavitation, thereby resulting in significant savings in computational time and resources.

4 Conclusion

In summary, a total of 12 CFD simulations using ANSYS Fluent are done to investigate the effects of: valve type, flow direction and valve opening on cavitation. Single-phase flow model is preferred for such an evaluation considering the number of simulations and the computational cost of a multiphase simulation. The performance of single-phase simulations are assessed previously in literature, and it is concluded that for a qualitative study such as this thesis work, it is not mandatory to enable the cavitation model when comparing two domains.

The prototype valve is designed to reduce cavitation around the throat section of the valve since it creates irreversible damage to components that are costly to substitute. For this reason, the new design implies the transportation of cavitation to a perforated cage which is easier and more economical to maintain, so that the pressure drop occurs in two steps in a more gradual way. However, prototype valve fails to do so because the area of the holes that are uncovered with the movement of the poppet are much smaller than the throat, considering how the flow enters the holes as well. Thus, the flow is constrained only at the holes of the cage, and the poppet must be elevated further to obtain the same flow rate as the commercial valve. Such behavior causes two types of response depending on the flow direction. In diverging flow, since the flow is not primarily restricted at the throat, and the pressure drop occurs downstream of the throat, where the cage and the outlet is connected, the cavitation tends to extend to the outlet, which is not observed for the commercial valve. Meanwhile, in converging flow, the response of the prototype valve is closer to the design objective because in this type of flow, at first, the fluid is decisively constricted in the holes of the cage, and then goes on to pass from the throat. Hence, a form of secondary restriction occurs, that helps to damp the cavitation extension to the outlet section.

Moreover, as the opening of the valve increases, cavitation tends to propagate more through the domain in both valves. Nonetheless, the magnitude of cavitation cannot be assessed by single-phase model, so it is unclear which case would have a more severe damage of cavitation.

4.1 Future work

The design of the prototype valve should be modified to create a double restriction as desired so that the pressure throughout the valve can be kept away from the water vapor pressure. The areas of the holes and the throat section can be made similar, considering the flow entrance to the tubes. The holes of the cage can be faced downwards to create a further pressure drop. Multiphase simulations can be conducted for all the lower opening cases since they are more critical for cavitation, as the single-phase simulation underestimates the cavitation extension and to obtain the physical flow rates for a quantitative study.

5 References

1- Krella, A. K. (2023). Degradation and protection of materials from cavitation erosion: A Review. *Materials*, *16*(5), 2058. https://doi.org/10.3390/ma16052058

2- Han, M., Liu, Y., Wu, D., Zhao, X., & Tan, H. (2017). A numerical investigation in characteristics of flow force under cavitation state inside the water hydraulic poppet valves. *International Journal of Heat and Mass Transfer*, *111*, 1–16. https://doi.org/10.1016/j.ijheatmasstransfer.2017.03.100

3- Bernad, S. I., & Susan-Resiga, R. (2012). Numerical model for cavitational flow in hydraulic poppet valves. *Modelling and Simulation in Engineering*, *2012*, 1–10. https://doi.org/10.1155/2012/742162

4- Oshima, S., Leino, T., Linjama, M., Koskinen, K. T., & Vilenius, M. J. (2001). Effect of cavitation in water hydraulic poppet valves. *International Journal of Fluid Power*, *2*(3), 05–13. https://doi.org/10.1080/14399776.2001.10781115

5- Amirante, R., Distaso, E., & Tamburrano, P. (2014). Experimental and numerical analysis of cavitation in hydraulic proportional directional valves. *Energy Conversion and Management*, *87*, 208–219. https://doi.org/10.1016/j.enconman.2014.07.031

6- Habibnejad, D., Akbarzadeh, P., Salavatipour, A., & Gheshmipour, V. (2022). Cavitation reduction in the globe valve using oblique perforated cages: A numerical investigation. *Flow Measurement and Instrumentation*, *83*, 102110. https://doi.org/10.1016/j.flowmeasinst.2021.102110

7- Yuan, C., Song, J., Zhu, L., & Liu, M. (2019). Numerical investigation on cavitating jet inside a poppet valve with special emphasis on cavitation-vortex interaction. *International Journal of Heat and Mass Transfer*, *141*, 1009–1024. https://doi.org/10.1016/j.ijheatmasstransfer.2019.06.105

8- Xu, H., Wang, H., Hu, M., Jiao, L., & Li, C. (2018). Optimal design and experimental research of the anti-cavitation structure in the water hydraulic relief valve. *Journal of Pressure Vessel Technology*, *140*(5). https://doi.org/10.1115/1.4040893

9- Wu, W., Qiu, B., Tian, G., Liao, X., & Wang, T. (2022). CFD-based cavitation research and structure optimization of relief valve for noise reduction. *IEEE Access*, *10*, 66356–66373. https://doi.org/10.1109/access.2022.3184449

10- Dastane, G. G., Thakkar, H., Shah, R., Perala, S., Raut, J., & Pandit, A. B. (2019). Single and multiphase CFD simulations for designing Cavitating Venturi. *Chemical Engineering Research and Design*, *149*, 1–12. https://doi.org/10.1016/j.cherd.2019.06.036

11- Ferrarese, G., Messa, G. V., Rossi, M. M., & Malavasi, S. (2015). New method for predicting the incipient cavitation index by means of single-phase computational fluid dynamics model. *Advances in Mechanical Engineering*, *7*(3). https://doi.org/10.1177/1687814015575974

12- Vallet, C., Ferrari, J., Rit, J.-F., & Dehoux, F. (2010). Single phase CFD inside a water safety valve. *ASME 2010 Pressure Vessels and Piping Conference: Volume 4*. https://doi.org/10.1115/pvp2010-25619

13- ANSYS Fluent Theory Guide

14- Zhang, L., Zhang, N., Peng, X., Wang, B., & Shao, X. (2015). A review of studies of mechanism and prediction of tip vortex cavitation inception. *Journal of Hydrodynamics*, *27*(4), 488–495. https://doi.org/10.1016/s1001-6058(15)60508-x

15- Paul, D., Agarwal, H., & Ponangi, B. R. (2020). CFD analysis of two-phase cavitating flow in a centrifugal pump with an inducer. *Heat Transfer*, *49*(6), 3854–3881. https://doi.org/10.1002/htj.21812